

Present-Day Atmospheric Simulations Using GISS ModelE: Comparison to In Situ, Satellite, and Reanalysis Data

GAVIN A. SCHMIDT,^a RETO RUEDY,^b JAMES E. HANSEN,^c IGOR ALEINOV,^a NADINE BELL,^a MIKE BAUER,^a SUSANNE BAUER,^a BRIAN CAIRNS,^a VITTORIO CANUTO,^c YE CHENG,^b ANTHONY DEL GENIO,^c GREG FALUVEGI,^a ANDREW D. FRIEND,^d TIM M. HALL,^c YONGYUN HU,^{a,*} MAX KELLEY,^d NANCY Y. KIANG,^a DOROTHY KOCH,^a ANDY A. LACIS,^c JEAN LERNER,^a KEN K. LO,^b RON L. MILLER,^c LARISSA NAZARENKO,^a VALDAR OINAS,^b JAN PERLWITZ,^f JUDITH PERLWITZ,^a DAVID RIND,^c ANASTASIA ROMANOU,^c GARY L. RUSSELL,^c MAKIKO SATO,^b DREW T. SHINDELL,^c PETER H. STONE,^f SHAN SUN,^g NICK TAUSNEV,^b DUANE THRESHER,^{a,†} AND MAO-SUNG YAO^b

^aNASA Goddard Institute for Space Studies, and Center for Climate Systems Research, Columbia University, New York, New York

^bNASA Goddard Institute for Space Studies, and SGT, Inc., New York, New York

^cNASA Goddard Institute for Space Studies, New York, New York

^dLSCE, CEA Saclay, Gif-sur-Yvette, France

^eNASA Goddard Institute for Space Studies, and Department of Applied Physics and Applied Mathematics, Columbia University, New York, New York

^fMassachusetts Institute of Technology, Cambridge, Massachusetts

^gNASA Goddard Institute for Space Studies, New York, New York, and Massachusetts Institute of Technology, Cambridge, Massachusetts

(Manuscript received 28 October 2004, in final form 6 March 2005)

ABSTRACT

A full description of the ModelE version of the Goddard Institute for Space Studies (GISS) atmospheric general circulation model (GCM) and results are presented for present-day climate simulations (ca. 1979). This version is a complete rewrite of previous models incorporating numerous improvements in basic physics, the stratospheric circulation, and forcing fields. Notable changes include the following: the model top is now above the stratopause, the number of vertical layers has increased, a new cloud microphysical scheme is used, vegetation biophysics now incorporates a sensitivity to humidity, atmospheric turbulence is calculated over the whole column, and new land snow and lake schemes are introduced. The performance of the model using three configurations with different horizontal and vertical resolutions is compared to quality-controlled in situ data, remotely sensed and reanalysis products. Overall, significant improvements over previous models are seen, particularly in upper-atmosphere temperatures and winds, cloud heights, precipitation, and sea level pressure. Data–model comparisons continue, however, to highlight persistent problems in the marine stratocumulus regions.

1. Introduction

General circulation models (GCMs) of the atmosphere–ocean–sea ice system are the laboratories with which climatologists experiment and hope to apply to understanding the real world (which remains significantly more complex than any model). These models contain, to the best of our ability, most of the processes that we believe to be important in determining climate.

The development of a GCM is a continual process of minor additions and corrections combined with the occasional wholesale replacement of particular pieces. In

* Current affiliation: Department of Atmospheric Sciences, Peking University, Beijing, China.

† Current affiliation: Department of Geosciences, and DFG Research Center Ocean Margins, University of Bremen, Bremen, Germany.

Corresponding author address: G. A. Schmidt, NASA Goddard Institute for Space Studies, and Center for Climate Systems Research, Columbia University, 2880 Broadway, New York, NY 10025.

E-mail: gschmidt@giss.nasa.gov

the case of Goddard Institute for Space Studies (GISS) series of models, the basic model description remained for many years the 1983 paper describing the then current model (Model II) (Hansen et al. 1983). A summary of the model version (Model II' ca. 1994) used in the Atmospheric Model Intercomparison Project (AMIP) experiments appears on the AMIP documentation Web site (Gates et al. 1999). Independent improvements in various modules (cloud physics, planetary boundary layer, ground hydrology, stratospheric dynamics, etc.) have been separately described (Del Genio et al. 1996; Hartke and Rind 1997; Rind et al. 1999; Rosenzweig and Abramopoulos 1997; Yao and Del Genio 1989; etc.). The prior frozen version of the model was denoted SI2000 and a brief description of that model was given in Hansen et al. (2002). Many innovations included in the current model were originally described in a coupled offshoot of the GISS model (Liu et al. 2003; Russell et al. 1995, 2000).

This paper is a description of the current version of the model (ModelE) and the development over recent years. As the direct successor model to both Model II and Model II', the current code could equally be denoted Model III. (Subsequent changes will be available at <http://www.giss.nasa.gov>.) Some studies discussing slightly earlier versions of ModelE have already appeared (Hansen and Nazarenko 2004; Mann and Schmidt 2003; Shindell et al. 2004), and much of the description here is valid for those results. The ModelE source code (along with documentation) can be downloaded from the GISS Web site (<http://www.giss.nasa.gov/tools/modelE>). Here, we will focus on the mean climatology of the atmospheric model and selected aspects of its intrinsic variability. Subsequent papers will discuss simulations of climate change since 1880, AMIP-style experiments, and fully coupled results and details of the specific tracer schemes and sensitivity studies of the physics. Relevant experiments using this model have been submitted for analysis as part of the Intergovernmental Panel on Climate Change 4th Assessment Report (IPCC AR4). Model results (including some of these other experiments) are available online (<http://www.giss.nasa.gov/data/>).

2. Model philosophy

The GISS model philosophy has always been to improve the physics of each modeled component, and to allow as great a degree as possible of flexibility in model configurations. This has led to a great deal of innovative and challenging science (Hansen and Nazarenko 2004; Hansen et al. 1997; Rind et al. 2001a,b, 1999; Shindell et al. 1999, 1998; and many others) al-

though some compromises (such as for horizontal resolution) were necessary. We have chosen not to uniquely pursue higher resolution, since that can severely limit the length and variability of the experiments possible, but rather we have maintained a variety of resolutions that can be used based on scientific need. Our experience has been that while some aspects of a simulation can be improved by increasing the resolution (frontal definition, boundary layer processes, etc.), many equally important improvements are likely to arise through improvements to the physical parameterizations. Indeed, some features (such as the stratospheric semiannual oscillation, high-latitude sea level pressure, or the zonality of the flow field) are degraded in higher-resolution simulations, indicating that resolution increases alone, without accompanying parameterization improvement, will not necessarily create a better climate model. As models improve and computer resources expand, there will always be a tension between the need to include more physics (tracers, a more resolved stratosphere, cloud microphysics, etc.), to run longer simulations, and to have more detailed vertical and horizontal resolution. The balance that is struck will be different for any particular application and so a flexible modeling environment is a prerequisite. In this paper, we therefore show results from three different configurations that differ principally in their horizontal and vertical resolution.

3. Model physics

The model physics are predominantly based on the physics of the GISS Model II' (SI2000 version) described in previous publications (Hansen et al. 2002, and references therein). However, many details have changed, and some physics has been completely reworked. We therefore provide a brief description of the current physics along with a summary of the major changes over the last few years. In all the subsequent text we are referring to the February 2004, ModelE1 public release version of the code.

In common with most other models, we make some basic assumptions at the outset, which though minor, have consequences throughout the model: namely, that water vapor does not add to atmospheric mass (i.e., globally integrated surface pressure is constant), the latent heat of atmospheric water vapor does not depend on temperature (i.e., all atmosphere-surface freshwater fluxes are assumed to be at 0°C), the potential energy of water vapor/condensate is neglected, condensate is not advected, and the pressure gradient calculation does not include humidity effects. We hope to be able to relax these constraints in future versions. The prin-

cial prognostic variables in the atmosphere are the potential temperature, water vapor mixing ratio, and the horizontal velocity components. Virtual potential temperature is used for all density/buoyancy-related calculations.

The advection is mass conserving for humidity and tracers, and potential enthalpy conserving for heat. All processes including the dynamics, cloud schemes, gravity wave drag, and turbulence conserve air, water, and tracer mass and energy to machine accuracy. All dissipation of kinetic energy through various mixing processes is converted to heat locally. In the long-term mean, the net flux of heat at the surface is equal to the net top-of-the-atmosphere (TOA) radiation. Angular momentum is conserved except due to drag and pressure torques at the solid land surface.

a. Configurations

The model has a Cartesian gridpoint formulation for all quantities. Available horizontal resolutions are $4^\circ \times 5^\circ$ and $2^\circ \times 2.5^\circ$ latitude by longitude (and $8^\circ \times 10^\circ$ for historical and pedagogical reasons). The effective resolution for tracer transport is significantly greater than these nominal resolutions because of the nine higher-order moments that are carried along with the mean tracer values in each grid box (see section 3d). The velocity points in the atmosphere are on the Arakawa-B grid and the vertical discretization follows a sigma coordinate to 150 hPa with constant pressure layers above. The standard vertical resolution has 20 layers and a model top at 0.1 hPa (Fig. 1). Compared to previous 12-layer versions (i.e., Hansen et al. 2002), the 20-layer code has 2 extra layers near the surface, 2 more in the lower stratosphere, and 4 extra layers above 10 hPa. We also describe a 23-layer version that better resolves the stratosphere and has a model top near the mesopause (≈ 0.002 hPa; Rind et al. 1999; Shindell et al. 1999).

The results described below are from three different configurations (Table 1): the $4^\circ \times 5^\circ$ 20-layer model (denoted M20), the corresponding full-stratospheric model (denoted M23, which differs in the vertical layering, model top, and use of a parameterized gravity wave scheme), and a simulation at $2^\circ \times 2.5^\circ$ (denoted F20) but which is identical to M20 in most other respects. The F20 simulation should be thought of as a sensitivity test to increased horizontal resolution, rather than a fully developed configuration (which continues to be worked on).

The surface is split into four types: open water (including lakes and oceans), ice-covered water (again including lake ice and sea ice areas), ground (including bare soil and vegetated regions), and glaciers. Within

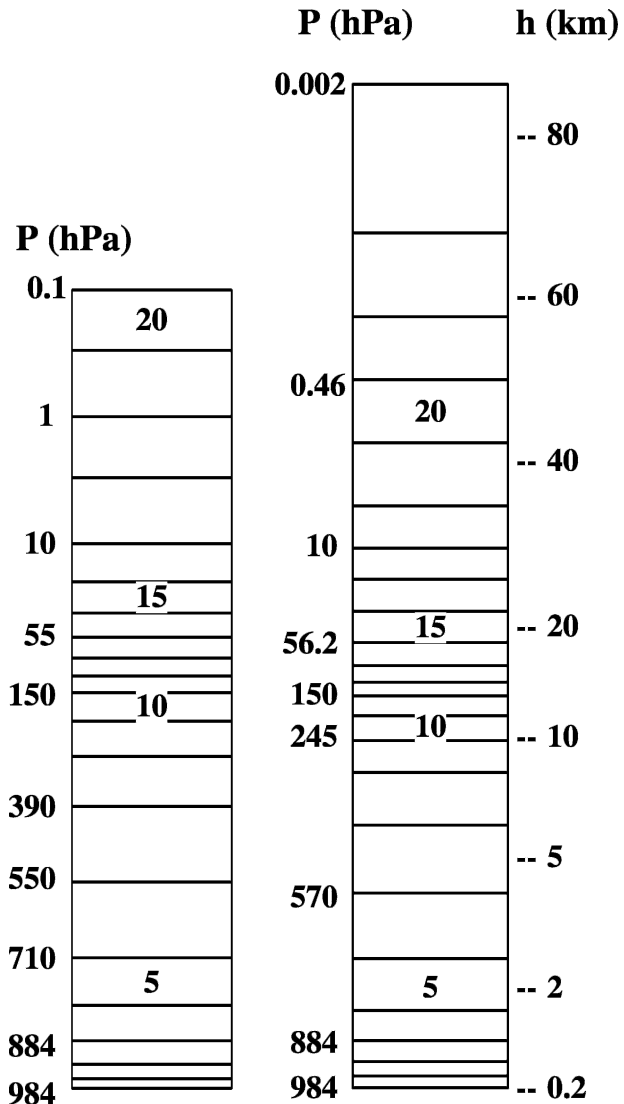


FIG. 1. Vertical layering for the 20- and 23-layer model configurations (for graphical convenience, the vertical coordinate shown here is linear in pressure to 150 hPa, logarithmic above).

each type there may be further subdivisions (fraction of plant functional types, fractional snow cover, melt pond fraction over sea ice, etc.), but those subdivisions are not seen by the atmospheric model except in weighted

TABLE 1. Model configurations. The effective tracer resolution takes into account the higher-order moments that are carried as part of the tracer advection scheme.

Model configuration	Horizontal resolution	Effective tracer resolution	Vertical layers	Model top (hPa)
M20	$4^\circ \times 5^\circ$	$\approx 1.3^\circ \times 1.6^\circ$	20	0.1
M23	$4^\circ \times 5^\circ$	$\approx 1.3^\circ \times 1.6^\circ$	23	0.002
F20	$2^\circ \times 2.5^\circ$	$\approx 0.7^\circ \times 0.8^\circ$	20	0.1
SI2000	$4^\circ \times 5^\circ$	$\approx 1.3^\circ \times 1.6^\circ$	12	10

mean quantities like the albedo. The model uses a 30-min time step for all physics calculations (compared to 1 h in previous model versions). The radiation code is called every five physics time steps (every 2.5 h) compared to every 5 h previously (however, the zenith angle is updated every time step).

b. Boundary conditions

For comparison with recent climatological data, all the results described here use 1979 boundary conditions including anthropogenic land use changes from conversion to cropland (Ramankutty and Foley 1999) and the spectrally discriminated solar irradiance (Lean 2000). Climatological (monthly varying) sea surface temperature (SST) and sea ice extent are averaged from 1975 to 1984 (Rayner et al. 2003). These fields are interpolated daily using a quadratic scheme that preserves the monthly mean value.

c. Atmospheric composition

Well-mixed trace gases [$(\text{CO}_2, \text{CH}_4, \text{N}_2\text{O},$ and chlorofluorocarbons (CFCs)] and all other elements of atmospheric composition used in the model—tropospheric and stratospheric ozone, the component of stratospheric water vapor derived from methane oxidation, stratospheric (volcanic) aerosols, and tropospheric aerosols [mineral dust, sea salt, sulfate, nitrates, organic carbon (OC), and black carbon (BC)]—are kept constant at 1979 levels for the experiments described here. Amounts of several dozen minor CFCs, HFCs, PFCs, HCFCs, and related compounds (Jain et al. 2000; Naik et al. 2000) are included in the form of (radiatively) equivalent amounts of CFC-11 and CFC-12. The stratospheric water source associated with methane oxidation is input using monthly varying latitude–height source functions derived from a 2D chemical transport model (Fleming et al. 1999). This source is proportional to the amount of CH_4 , lagged by 2 yr. Volcanic aerosols are as described in Hansen et al. (2002). For the tropospheric aerosols and ozone, we use model-generated 3D fields from the SI2000/Model II' series of experiments as described below.

1) OZONE

Tropospheric ozone is prescribed according to chemistry–climate simulations with the previous version of the GISS GCM (Shindell et al. 2003). A 3D monthly mean stratospheric ozone climatology is constructed from four different data sources. The basic structure for stratospheric ozone is obtained from the zonally averaged monthly mean climatology constructed by G. La-

bow (2004, personal communication) from 15 yr of ozonesonde measurements merged with Stratospheric Aerosol and Gas Experiment (SAGE, version 6.1) and Upper Atmosphere Research Satellite–Microwave Limb Sounder (UARS–MLS) data for the 15-yr period from 1988 to 2002. Superimposed on the Labow climatology is the Randel and Wu (1999) stratospheric ozone trend for the period 1979 to 1997. Above the 1-hPa level extending to 0.001 hPa, we use the monthly mean middle-atmosphere ozone distribution from Keating and Young (1985). Following Hansen et al. (2002), we define the boundary between stratospheric and tropospheric ozone as occurring at the 150-hPa level in the Tropics, decreasing to 200 hPa between -45° and 60° and then dipping to 290 hPa poleward of 60° . In the Antarctic and Arctic, the Randel and Wu trend is extrapolated downward to the surface and merged smoothly with the Shindell tropospheric ozone at -60°S and 60°N . The ozone time series is renormalized so that ozone averaged over the 1988 to 2002 time period reproduces the Labow climatology.

In the polar regions, there is a pronounced longitudinal (and seasonal) variation in column ozone associated with the planetary stationary waves of each hemisphere. We take the normalized longitudinal variability from the London monthly mean total ozone climatology (London et al. 1976) and apply it to our Labow-based stratospheric ozone distribution. This has the effect of slightly increasing the stationary wave energy in model.

2) TROPOSPHERIC AEROSOL DISTRIBUTION

The geographic and particle size distribution of mineral dust aerosol is identical to that used by Hansen et al. (2002), derived from Tegen et al. (1997). The distribution originates from both natural and anthropogenic sources that together contribute to global annual emission of roughly 1300 Tg. The dust index of refraction is specified using laboratory measurements at solar (Patterson et al. 1977) and thermal (Volz 1973) wavelengths of Saharan dust particles collected at Barbados, with two exceptions. First, solar absorption is reduced using the imaginary index of refraction inferred by Sinyuk et al. (2003), based upon Total Ozone Mapping Spectrometer (TOMS) retrievals and measurements by Aerosol Robotic Network (AERONET) sun photometers. Outside of the visible wavelengths considered by that study, the imaginary index is extrapolated to join smoothly with the Volz values at $2\text{ }\mu\text{m}$. Second, scattering at thermal wavelengths, although not explicitly computed, is represented by a 30% increase in optical thickness, as suggested by the calculations of Dufresne et al. (2002). Compared to the dust radiative forcing

included in SI2000, these two modifications result in a near doubling of the (negative) TOA forcing, with a reduction in the magnitude of surface forcing by roughly one-third (Miller et al. 2004).

The sulfate and carbonaceous aerosol fields were generated by the model (SI2000 version; Koch 2001; Koch et al. 1999) with industrial SO_2 emissions based on the inventory of Lefohn et al. (1999). Industrial black carbon emissions for 1950 to 1990 are based on United Nations energy statistics as described in Tegen et al. (2000). However, emission factors are from Cooke et al. (1999); power plant emission factors for hard and brown coal (0.05 g kg^{-1}) are from Tami Bond as cited in Cooke et al. (1999). Emissions were adjusted based on time-dependent technology factors for western countries from Novakov et al. (2003), including neighboring countries to those considered in that study. Organic carbon emissions are assumed to be a factor of 4 and 7.9 times the BC emissions for industrial and biomass, respectively (Liousse et al. 1996). Natural and biomass burning emissions are as described in Koch et al. (1999) and Koch (2001). The BC and OC obtained from the aerosol transport model are multiplied by factors of 1.9 and 2.5, respectively, in order to obtain aerosol absorption indicated by AERONET (Sato et al. 2003). Biomass burning BC and OC are assumed to increase linearly from one-half of the present-day amount in 1850 to the present-day amount in 1990. Further details of the time dependence of these aerosol fields can be found in Hansen et al. (2005).

3) TROPOSPHERIC AEROSOL TREATMENT

Hygroscopic aerosols (i.e., sulfates, nitrates, sea salt, and organic carbon) increase in size as the relative humidity increases, which increases the aerosol scattering efficiency and radiative forcing (Boucher and Anderson 1995; Nemesure et al. 1995; Tang et al. 1981). This increase in particle size has been accurately measured in the laboratory and parametric formulas derived to express the particle growth as a function of relative humidity, as well as the accompanying change in density and refractive index as the initially solid particle dissolves and takes on water (Tang 1996; Tang and Munkelwitz 1991, 1994; Tang et al. 1981). Typically, a particle remains solid until the relative humidity reaches a critical value of deliquescence whereupon it rapidly dissolves and increases in size with increasing relative humidity. As relative humidity decreases, solute particles follow the equilibrium curve until relative humidity falls below the crystallization point, whereupon it rapidly loses its water and makes a rapid transition to its dry crystalline state. The dominant effect is

a strongly nonlinear increase in aerosol optical depth as relative humidity increases, particularly for relative humidities above 0.9. However, the extinction efficiency of a hygroscopic aerosol may either increase or decrease with relative humidity, depending on the effective radius of the dry seed size. Based on these laboratory measurements, hygroscopic aerosol radiative properties depend explicitly on the local relative humidity and fully include the effects of changing refractive index and droplet size on the aerosol Mie scattering properties.

We parameterize this in terms of an external mixture of the dry aerosol and a pure water aerosol of appropriate size with the sizes set to reproduce precisely the extinction efficiency and asymmetry parameters of the solute aerosol at the laboratory wavelength of 633 nm. We have found that the spectral dependence of aerosol radiative parameters is retained by the external mixture with excellent accuracy. Look-up tables of Mie scattering coefficients are tabulated for relative humidities ranging from 0 to 0.999 separately for each aerosol type with dry aerosol seed sizes set at model initialization within the range of 0.1- to $10\text{-}\mu\text{m}$ effective radius.

The evaluation of the resulting aerosol optical thickness is shown in Fig. 2. We compare 1990 conditions (the latest period for which emissions were available) to the mean Moderate Resolution Imaging Spectroradiometer (MODIS) results from 2001–03. This comparison is principally an evaluation of the (fixed) aerosol mass field and mean relative humidity in the model. Clear-sky values are the most appropriate comparison to the satellite observations, while total-sky values are significantly higher (due to the correlation of clouds with higher relative humidity). The amounts of all of these aerosols are moderately less in 1979 than in 1990, the global mean clear-sky aerosol optical depth at 550 nm being 0.13 in 1979 compared with 0.14 in 1990. The 1979 values are used in the model simulations described here.

d. Dynamics

The runs described here use a second-order scheme for the momentum equations. Tracers, including heat and humidity, are advected using the highly nondiffusive Quadratic Upstream Scheme (QUS; Prather 1986), which keeps track of nine subgrid-scale moments as well as the mean within each grid box. This increases the effective resolution of the tracer fields (Table 1) and allows the GISS series of models to produce reasonable climate fields with relatively coarse nominal resolution. The physics routines (principally due to moist convection) modify the tracer moments consistently, although the subgrid-scale information is not yet

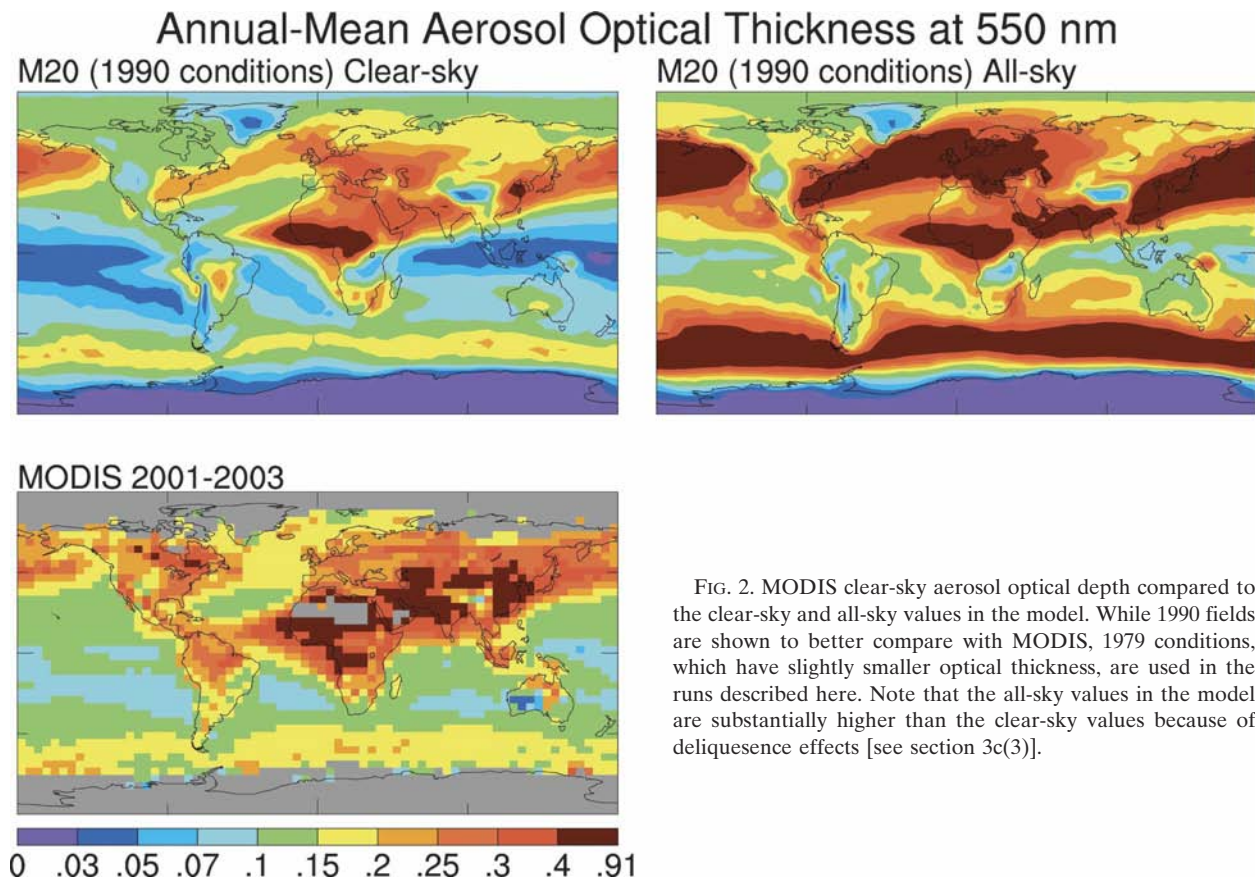


FIG. 2. MODIS clear-sky aerosol optical depth compared to the clear-sky and all-sky values in the model. While 1990 fields are shown to better compare with MODIS, 1979 conditions, which have slightly smaller optical thickness, are used in the runs described here. Note that the all-sky values in the model are substantially higher than the clear-sky values because of deliquescence effects [see section 3c(3)].

used, for instance, to initiate convection. A small correction to the QUS advection was made (with little impact on the results). We ensure that the loss of potential energy is exactly balanced by the gain in kinetic energy using a small global correction to the temperature.

The basic dynamics code has not changed substantially since SI2000; however, there have been a number of modifications that aimed to increase the computational efficiency of the dynamical core and its accuracy and stability at the Poles. Substantial effort has also been made to make the effects of physics routines on the subgridscale moments more consistent with the effects on the mean profile. This has led to reduced noise, particularly due to the subsidence and mixing in the convection routines.

The advection of humidity (and other tracers) is done only once every physics time step (30 min) with iterative time stepping to avoid any Courant–Fredrichs–Levy violations. The smaller time steps are used primarily in the stratosphere and upper troposphere where zonal winds are strong or as a result of extremely high flow deformation. Occasionally, divergence along a particular direction might lead to temporarily nega-

tive gridbox masses. These exotic circumstances happen rather infrequently in the troposphere but are common in stratospheric polar regions experiencing strong accelerations from parameterized gravity waves and/or Rayleigh friction. Therefore, we limit the advection globally to prevent more than half the mass of any box being depleted in any one advection step.

At the velocity grid points surrounding the polar caps, first-order errors in the calculation of the pressure gradient force, horizontal momentum advection, and the Coriolis force in Model II' were corrected. Momentum tendencies due to the pressure gradient force and horizontal advection were previously underestimated as a result of an overestimate of gridbox areas at this latitude. For grids that do not have a half box at the Pole (i.e., the GISS $8^\circ \times 10^\circ$ or $2^\circ \times 2.5^\circ$ grids) additional adjustments to the calculation of air mass fluxes, the pressure gradient force, and momentum advection were necessary to maintain second-order accuracy of these terms at the Poles.

An additional issue that becomes increasingly important at high latitudes is the desirability that the schemes for the metric term and momentum advection be sufficiently consistent to ensure that the sum of these terms

would be zero, for radial geometry, in a region of spatially constant absolute velocity (i.e., the streamfunction varies linearly with respect to the components of a Cartesian coordinate system). At all latitudes, the nonlocal mass flux stencil for the metric term as implemented in the GISS code allows the metric and advective tendencies to be slightly inconsistent when surface pressure varies in the σ coordinate. This nonlocality is particularly problematic for the row of velocities encircling the polar cap, since the east–west mass fluxes within the polar cap are not calculated from the appropriate local velocities but are constructed instead to satisfy mass balance for velocity grid boxes overlapping a homogenized polar cap. To solve this problem at the Pole, we simply eliminate the need for the metric term by computing, for the polar velocity row only, the advective tendency of the Cartesian component velocity field and then transforming the result back to spherical-grid components. Finally, for physical accuracy, the Coriolis force is applied at full strength in the polar velocity rows, reversing the practice of zeroing out the Coriolis force at the Pole in Model II' that was in keeping with the original Arakawa (1972) B-grid scheme. These changes have limited impacts on the solution away from the polar region.

The above changes improve computational accuracy, but they do not eliminate polar instabilities associated with large Courant numbers for the zonal advection of momentum where winds are strong. In ModelE we apply a longitudinal diffusion directly to the velocity field at latitudes poleward of $\approx 80^\circ$, to eliminate these instabilities. The diffusion acts in addition to the velocity filtering employed at all latitudes to remove two-gridpoint noise. The value of the diffusion coefficient K depends upon zonal wind speed. In velocity rows for which the maximum zonal Courant number is less than one-half, K is set to $10^3 \text{ m}^2 \text{ s}^{-1}$, a value that requires $t = \Delta x^2 K^{-1} \approx 1$ day to act over a near-polar grid spacing Δx on the order of 10 km but an essentially infinite time to affect synoptic scales of 1000 km. As the Courant number increases from one-half to unity, K increases linearly from $10^3 \text{ m}^2 \text{ s}^{-1}$ to a maximum of $10^7 \text{ m}^2 \text{ s}^{-1}$. To avoid spurious drag upon the spatially constant part of transpolar flow, the velocity field is temporarily transformed into Cartesian components to apply this procedure. In Model II' the zonal component of mass fluxes and the pressure gradient force near the Pole were instead smoothed in the zonal direction, but this retained the noise in the velocity field.

A final change to the dynamical core attempts to diminish the impact of computational errors in regions of steeply sloping topography, over which horizontal and vertical airmass fluxes are convolved as a result of

the GCM's use of the terrain-following σ coordinate. "Horizontal" winds in the σ coordinate, which evolve according to horizontal pressure gradients (that are arguably inaccurate around steep topography), correspond to a vertical mass flux over sloping topography even though they are within a hydrostatic model in which vertical motions should have no prognostic component. At the horizontal resolution of the GISS GCM, horizontal flow within a single σ level can raise air from low to high elevations, which has profoundly negative effects upon the model's hydrology in some areas. In an extreme example, the tropical easterlies lift moist boundary layer air from the Amazon to Andean elevations over a distance of 1 grid box, generating a "bull's-eye" of intense convection over the Andes, which preferentially draws moisture that should be maintaining Amazonian convection. To ameliorate the situation without drastically altering the structure of the GCM, upslope flow in the σ -horizontal direction was made to explicitly rise in the vertical direction to the surface altitude of the downwind grid box before continuing to that grid box. This procedure conserves the column-integrated horizontal mass flux but essentially transfers flux from lower to higher layers. While creating some spurious downward velocities at the downwind grid box as a result of the continuity equation, this somewhat arbitrary choice prevents spurious upslope moisture transport and greatly improves the rainfall distribution over the Amazon, with obvious consequences for downwind areas whose moisture is derived from Amazonian convection. Globally, few regions other than the Andes, the Himalayas, the Alaskan coastal range, Greenland, and Antarctica have sufficiently steep topography to be directly affected by this change, and excessive high-altitude precipitation is reduced or eliminated at all these locations.

e. Stratospheric and gravity wave drag

For numerical stability, ModelE applies an empirical Rayleigh drag scheme at the model top: $\tau = -\rho C_D |U|U$, where ρ is the air density, U is the horizontal velocity vector, and the drag coefficient C_D is given by

$$C_D = \mu \left(\frac{V_c}{|U| + V_c} \right)^2 (1 + \gamma |U|), \quad (1)$$

with $V_c = 30 \text{ m s}^{-1}$ (a typical critical wind speed for stratospheric conditions) and tunable constants γ and μ . This differs from previous versions in that the effectiveness of the drag is maximized at the critical wind speed, more in keeping with the physical behavior of actual gravity waves.

In the middle atmosphere, ModelE can either use an

TABLE 2. Stratospheric drag treatment in the current and previous configurations.

Model configuration	Top-layer drag	Interior drag	Simple drag coefficients	Full GWD coefficients*
M20	$\gamma = 0.1, \mu = 0.002$	Simple	$\gamma = 0, \mu = 0.0002$	—
M23	$\gamma = 0.1, \mu = 0.0002$	Full GWD	—	200 hPa, $3 \times 10^{-5}, 3 \times 10^{-7}$
F20	$\gamma = 0.1, \mu = 0.004$	Simple	$\gamma = 0, \mu = 0.0004$	—
SI2000**	$\gamma = 0.1, \mu = 0.0005$	None	—	—

* Tunable factors for defining the generation of gravity waves and their magnitude: Pressure level above which gravity waves break, deformation threshold (s^{-1}), and mountain wave factor.

** In SI2000, the top-layer drag coefficient had a simpler formulation: $C_D = \mu(1 + \gamma|U|)$.

extension of this simple scheme or a climate-dependent gravity wave drag (GWD) scheme (Rind et al. 1988). For M23 (and other configurations with similarly high model tops) the full GWD scheme is required, though for the models with tops near 0.1 hPa (M20 and F20), we apply the simple scheme above 150 hPa. The full GWD scheme separately calculates the effects of gravity waves arising from mountain drag, penetrating convection (above 400 hPa), shear, and deformation. Changes in the stratospheric angular momentum due to the GWD or Rayleigh drag are balanced locally by a (small) correction in the troposphere, mimicking in some way the transfer of momentum by the (unresolved) gravity waves. Older versions of the model did not conserve angular momentum in these processes. Table 2 shows the constants used in the current configurations, chosen to give the best approximation to the mean zonal wind field and its variability in the upper atmosphere.

f. Radiation

The radiation model is basically as described by Hansen et al. (1983), with explicit multiple scattering calculations for solar radiation [shortwave (SW)] and explicit integrations over both the SW and thermal [longwave (LW)] spectral regions. Gaseous absorbers of SW radiation are H_2O , CO_2 , O_3 , O_2 , and NO_2 . Size-dependent scattering properties of clouds and aerosols are computed from Mie scattering, ray tracing, and T-matrix theory (Mishchenko et al. 1996) to include non-spherical cirrus and dust particles. The k -distribution approach (Lacis and Oinas 1991) utilizes 15 noncontiguous spectral intervals to model overlapping cloud-aerosol and gaseous absorption. The surface albedo utilizes six spectral intervals and is solar zenith angle dependent for ocean, snow, and ice surfaces. The spectral albedo of vegetation is seasonally dependent. The radiation model generates spectrally dependent direct/diffuse flux ratios for use in biosphere feedback interactions.

Longwave calculations for H_2O , CO_2 , and O_3 use the

correlated k distribution with 33 intervals (Lacis and Oinas 1991; Oinas et al. 2001), designed to match line-by-line computed fluxes and cooling rates throughout the atmosphere to within about 1%. Weaker bands of H_2O , CO_2 , and O_3 , as well as absorption by CH_4 , N_2O , CFC-11, and CFC-12 are included in an approximate fashion as overlapping absorbers, but with coefficients tuned to reproduce line-by-line radiative forcing over a broad range of absorber amounts. The vertical profiles and latitudinal gradients of CH_4 , N_2O , and CFCs are from Minschwaner et al. (1998). Longwave forcing by aerosols is also included (Tegen et al. 2000).

Thermal fluxes are calculated using a no-scattering format with parameterized correction factors applied to the outgoing TOA flux to account for multiple scattering effects using tabulated data from offline calculations. Longwave multiple scattering increases the cloud thermal greenhouse contribution by reducing the global outgoing TOA flux by about 1.5 W m^{-2} . Multiple scattering by clouds also increases the global mean downwelling flux at the surface by about 0.4 W m^{-2} compared to the no-scattering approximation. While the magnitude of the cloud multiple scattering effect has been reported in the literature to be as large as 20 W m^{-2} (Chou et al. 1999; Edwards and Slingo 1996; Ritter and Geleyn 1992; Stephens et al. 2001), our calculations show this to be an overestimate because these earlier studies defined their no-scattering reference by setting the single scattering albedo to zero. A better no-scattering approximation is achieved by setting the asymmetry parameter to unity so that the cloud particle absorption cross section (rather than the extinction cross section) is used in subsequent radiative transfer calculations (Paltridge and Platt 1976). The LW forcing due to well-mixed greenhouse gases compares very well to line-by-line calculations, differing by less than 1% at the TOA and only slightly more at the surface. These results have been submitted as part of the radiative transfer model intercomparison project for IPCC AR4 and are available on the ModelE Web site.

The radiation model also includes the effects of 3D

cloud heterogeneity via the Cairns et al. (2000) 3D cloud parameterization in order to get more realistic albedos from realistic water paths and particle sizes. The procedure retains the use of plane-parallel homogeneous layer geometry and works by rescaling the plane-parallel cloud parameters (optical depth, asymmetry parameter, and single scattering albedo) according to the relative variance of the cloud particle density distribution and is based on rigorous theoretical analysis and Monte Carlo simulations. Global maps of monthly mean cloud particle density distribution have been derived from the International Satellite Cloud Climatology Project (ISCCP) D1 cloud climatology (Rossow et al. 2002) and are incorporated in the prognostic cloud optical parameters to simulate subgrid cloud optical depth distributions in accordance with the observed cloud relative variances. Cloud overlap, which the GISS radiation scheme represents in the time domain, is now assumed to be mixed maximum-random, compared to maximum overlap previously.

The spectral and solar zenith angle dependence of ocean albedo is based on calculations of Fresnel reflection from wave surface distributions as a function of wind velocity (Cox and Munk 1956). The effects of foam and hydrosols on ocean albedo are also included (Gordon and Jacobs 1977). The spectral and solar zenith angle dependence of snow and sea ice is modeled in accordance with the scheme described by Warren and Wiscombe (1980). Snow “ages” following the prescription of Loth and Graf (1998) and has a different albedo for wet or dry snow. Ocean ice albedo is spectrally dependent and is a function of ice thickness and parameterized melt pond extent [Ebert et al. (1995); Schramm et al. (1997), with modifications from C. M. Bitz (2004, personal communication)].

g. Cloud processes

The cumulus and stratiform cloud parameterizations in the model are similar in most respects to those described in Del Genio and Yao (1993) and Del Genio et al. (1996). The model uses a mass flux approach to cumulus parameterization with one undiluted and one entraining plume. Convection can be triggered at any model level when an air parcel, lifted one model layer, saturates and becomes buoyant, based on a virtual moist static energy criterion. The mass flux closure assumes that enough mass is transported in a model physics time step to produce neutral buoyancy of lifted parcels at cloud base; this allows boundary layer relative humidity and free-troposphere lapse rate to vary in quasi-equilibrium fashion. Cumulus downdrafts are produced for parcels rising more than one model level at the first level at which an equal mixture of cloud and

environmental air is negatively buoyant. The downdraft penetrates (potentially below the cloud base) until negative buoyancy is eliminated, evaporating precipitation to the extent required to maintain saturation. Downdraft mass flux is assumed to be one-third the updraft mass flux at the formation level. Downdrafts now include entrainment at the same fractional rate (0.2 km^{-1}) as entraining updrafts. The undiluted fraction of the cumulus mass flux now entrains below the 800-hPa level. Cumulus condensate is detrained into an anvil whose evolution is treated similarly to stratiform clouds. Convective cloud cover is treated diagnostically as the fraction of the mass of a gridbox that convects, with additional cloudiness above the freezing level assumed for a single time step when convection detrains into a dry environment that cannot support an evolving stratiform anvil. Subsidence is now performed using QUS advection (as opposed to a simple upwind scheme).

Stratiform cloud water is treated prognostically, with cloud formation based on the available moisture convergence following Sundqvist (1978) and Sundqvist et al. (1989). A single cloud water variable is predicted; its phase is diagnosed as a function of temperature with a correction for glaciation of supercooled water by precipitation falling from above. Stratiform cloud volume fraction is a diagnostic function of relative humidity above a tunable threshold value U_{00} . Cloud areal fraction is predicted from cloud volume fraction according to the stability of the model layer, with partial layer cloudiness permitted in the vertical as well as the horizontal. The scheme includes simple representations of all microphysical sources and sinks of cloud water, including autoconversion, accretion, evaporation, and Bergeron–Findeisen growth via the seeder–feeder process. Convective detrainment is an additional source of cloud water, while cloud-top entrainment, at a rate diagnosed by a cloud-top interface stability criterion, is a cloud water sink. Cloud droplet effective radius is diagnosed from the cloud water content assuming constant number concentration in standard versions of the model, but with different number concentrations for liquid clouds over land and ocean and also for ice clouds. In versions of the model that calculate the indirect effect of aerosols, droplet number concentration is interactive instead (Menon et al. 2002). The droplet effective radius for calculating optical thickness is based on a droplet size distribution with effective variance 0.2 (rather than using the volume mean radius), and is limited to $20 \text{ }\mu\text{m}$ for heavily precipitating liquid clouds. Cloud optical thickness is diagnosed interactively from the variable droplet effective radius and subgrid vertical cloud thickness. Note that throughout the cloud pa-

parameterization, we maintain local conservation of air mass, energy, water, and tracers.

We have implemented a new microphysics scheme to handle the partitioning between convective precipitation and detrainment into anvil clouds for deep convective events. For this purpose convective condensate is assumed to be liquid below the freezing level and a graupel-ice mixture above. We partition the condensate in each layer into a precipitating and a nonprecipitating part by making three assumptions: (i) there is a Marshall-Palmer drop size distribution (DSD) with intercept value $8 \times 10^6 \text{ m}^{-4}$, a typical value for storm systems (Marshall and Palmer 1948); (ii) for the particle size-fall speed relationships, we use a fit to the pressure-adjusted terminal velocity measurements of Gunn and Kinzer (1949) for liquid droplets (Fowler et al. 1996), a pressure-adjusted version of the Locatelli and Hobbs (1974) relationship for lump graupel, and a similar relation given by Rutledge and Hobbs (1984) for ice/snow; and (iii) cumulus updraft speed profiles $w_c(p)$ between 400 and 700 hPa are specified as 2 and 5 m s^{-1} for nonentraining updrafts over ocean and land, respectively, and half those values for entraining plumes, based loosely on observations (Lucas et al. 1994). Above and below these levels updraft speeds decrease linearly to zero at the surface and top of the atmosphere. We solve for the critical diameter D_c at which its terminal velocity equals w_c . The amount of convective condensate converted to precipitation in each layer is then defined as the part of the mass distribution with $D > D_c$, and the remainder of the convective condensate in each layer is assumed to be detrained. Above the freezing level, ice/snow and graupel are partitioned linearly with respect to layer temperature, with 100% ice for $T = -40^\circ\text{C}$ and below. This replaces the previous scheme in which a fixed fraction of the convective condensate above the 550-hPa level [100% in Del Genio et al. (1996) and 50% in SI2000] was detrained.

The model allows for a reasonable probability of supercooled cloud water at temperatures not too far below freezing and assumes that the autoconversion of such condensate produces supercooled liquid precipitation. In reality as droplets grow to precipitation size, the probability of glaciation significantly increases. To avoid excessive occurrence of freezing rain at the surface, we define a probability function

$$P_f = (1 - \exp[(T - 273.16)/C]) \max(D\mu/\mu_r, 1), \quad (2)$$

where T is temperature in kelvins, μ is cloud water content, and μ_r is the critical cloud water content for effective autoconversion defined in Del Genio et al.

(1996). We set $C = 2.5 \text{ K}$ and $D = 10$, which gives a reasonable frequency of snow rather than freezing rain at the ground. Previously the phase of precipitation was determined from the surface temperature, but this led to a nonconservation problem with the latent heat, which is remedied by the new procedure.

Relative to SI2000, ModelE includes several additional significant changes [described more fully in Del Genio et al. (2005a)]. Grid boxes are now divided into subgrid convective (updraft and subsidence, assumed to have equal area) and nonconvective (cloudy and clear sky) parts. Stratiform cloud formation below the cumulus detrainment level is restricted to the nonconvective portion of the gridbox. This has the beneficial effect of suppressing some of the excessive low cloud in tropical convective regions, and it thus permits the stratiform cloud scheme's threshold relative humidity to be lower than would otherwise be the case, thereby increasing cloud somewhat in the eastern ocean marine stratocumulus regions while maintaining global radiative balance. An improved atmospheric turbulence scheme is used (see below), which leads to water vapor being effectively vented from the lowest model layer, eliminating the need (as in SI2000) for a separate threshold humidity calculation to avoid excessive first-layer cloudiness. Separate equations relating stratiform cloud cover to clear-sky relative humidity, and clear-sky humidity to a threshold relative humidity, at different points in the code were combined into a single equation, reducing high-frequency noise in cloud cover. Threshold liquid water contents for efficient precipitation were halved for liquid phase stratiform clouds. Cloud morphology was originally specified to allow stratiform clouds to fill the grid box horizontally but not vertically under stable conditions, but in the current version the maximum horizontal cloud fraction is less than 100% unless the grid box is saturated.

In the formulation of the gridbox mean relative humidity tendency [Eq. (5) in Del Genio et al. (1996)], we now eliminate cloud water evaporation (E_c) as a sink of cloud water content to be consistent with Sundqvist's formulation, which includes this effect only to the extent that cloud water is advected from an adjoining gridbox (which does not occur in ModelE). A small effect of E_c on the maximum possible size of cloud droplets remains.

The parameterization of the evaporation (sublimation) of stratiform precipitating water droplets (ice crystals) was modified to include a length scale and a different dependence upon relative humidity. According to the Sundqvist (1978) prescription adopted by Del Genio et al. (1996), the diminution ΔP of precipitation rate P as hydrometeors fall from the top to the bottom

of a layer is simply proportional to the layer's subsaturation ($1 - U$), where U is the relative humidity, but independent of the physical thickness of the layer Δp in pressure units. This has the undesirable result that the evaporative moistening rate $g\Delta P/\Delta p$ increases with the vertical resolution of the model, subsaturations being equal. Therefore, the calculation was altered so that the attenuation of P contains a proportionality to layer thickness:

$$\Delta P = -P \min[(\Delta p/\Delta p_{\text{evap}})(1 - U)^n, 1]. \quad (3)$$

The reference scale Δp_{evap} was chosen to be 100 hPa, comparable to the average vertical resolution of the GCM configuration in which the cloud scheme was originally developed. We set $n = 2$ (compared to $n = 1$ previously), which improves the simulation of Amazon basin rainfall and reduces the possibility of excessive evaporative cooling of the layer in a single time step.

The model is tuned (using the threshold relative humidity U_{00} for the initiation of ice and water clouds) to be in global radiative balance (i.e., net radiation at TOA within $\pm 0.5 \text{ W m}^{-2}$ of zero) and a reasonable planetary albedo (between 29% and 31%) for the control run simulations. In these experiments we use $U_{00} = 0.59, 0.57$, and 0.59 for ice clouds and $0.82, 0.82$, and 0.83 for water clouds in M20, F20, and M23, respectively.

h. Atmospheric turbulence

ModelE uses a calculation of atmospheric turbulence over the whole column. This replaces dry convective adjustment, which was used to deal with static instabilities in Model II'.

In the atmospheric planetary boundary layer (PBL), we use a formulation for the temperature, moisture, and scalar fluxes that consists of a local (diffusive) term and a countergradient term derived from large-eddy simulation (LES) data (Holtslag and Moeng 1991). We also use the formulation for the turbulent kinetic energy derived by Moeng and Sullivan (1994) from their LES data. The countergradient term is scaled by the surface flux of each quantity and effectively distributes that flux over the PBL according to a parameterized profile (Holtslag and Moeng 1991). This profile depends on the height of the PBL, which is closely related to the large eddy size and thus characterizes the non-locality, and the buoyancy and shear effects at the surface. Results show that the nonlocal turbulence model effectively raises the maxima of the relative humidity (and hence cloud cover) in the Tropics from the lowest atmospheric layer to about 900 hPa (corresponding to layer 3 in the standard 20-layer resolution), which is more consistent with observations.

Above the PBL we use the second-order closure (SOC) model developed by Cheng et al. (2002), which is a natural generalization and improvement of the original SOC model of Mellor and Yamada (1982). The Reynolds stress and heat flux equations have been solved with more advanced parameterization of the pressure–velocity and pressure–temperature correlations. In addition, a few turbulent time scales are determined by a new two-point turbulence closure model (Canuto and Dubovikov 1996a,b). The most noticeable improvement is the increase in the critical Richardson number (beyond which turbulence in stable conditions ceases to exist) from 0.2 to 1. Under unstable conditions, the model compares more favorably with the Kansas data as analyzed by Businger et al. (1971) and Hogstrom (1988). The length scale, which extends smoothly from within the PBL to the free atmosphere, is taken from Holtslag and Boville (1993).

i. Surface fluxes

The surface fluxes are calculated using a submodule that is embedded between the surface and the midpoint of the first resolved model layer. A level-2.5 turbulence model (Cheng et al. 2002) is applied to this region (using eight sublayers) independently over each surface type. The lower boundary conditions for the wind and the potential temperature equations are determined assuming continuity of the respective turbulent fluxes at the surface. To calculate the fluxes through the surface layer, drag and transfer coefficients are set using similarity theory following Hartke and Rind (1997). The roughness length for momentum (z_{0m}) over land is specified as in Hansen et al. (1983). The roughness lengths for temperature (z_{0h}) and moisture (z_{0q}) over land and land ice are taken from Brutsaert (1982) to be proportional to z_{0m} . Ocean and ocean ice are treated as rough bluff surface, with z_{0m} combining the smooth surface value (Brutsaert 1982) with the Charnock relation for the aerodynamic roughness length; as for z_{0h} and z_{0q} Eqs. (5.26)–(5.27) of Brutsaert (1982) with background values 1.4×10^{-5} and $1.3 \times 10^{-4} \text{ m}$, respectively, are used.

We reduce the saturation specific humidity by 2% over the oceans (to account for sea salt aerosol effects; Gill 1982). Over land, the surface evaporative flux is determined by the vegetation, but to improve estimates of surface humidity by the submodule described above, we calculate the maximum available evapotranspiration and do not allow the atmosphere to draw more water than is available. This requires a change in the humidity surface boundary condition from a variable to a fixed flux in such situations.

j. Land surface

The land surface model used in ModelE consists of three integrated parts: soil, canopy, and snowpack. It is based primarily on Rosenzweig and Abramopoulos (1997) with various modifications and improvements. In particular, these include the implementation of a three-layer snow model, addition of new algorithms for the underground runoff computation, and inclusion of elements of new vegetation biophysics. The snow and land surface code conserve water and energy up to machine accuracy.

1) SNOW AND HYDROLOGY

In the snow model the snowpack is represented by three layers of snow (Lynch-Stieglitz 1994), which can collapse to one layer for a very thin snowpack. At each time only a fraction of the GCM cell is covered by the snow. This snow fraction f_{snow} depends on the amount of snow in the cell but is reduced over rough topography using the formulation of Roesch et al. (2001). The snow is located between the canopy and the soil, but for thick snowpack, part of the snow can rise above the canopy and cover it completely (the “vegetation masking” effect).

Each layer of the snow in the model is described by three prognostic variables: the amount of snow water W_i in the layer in meters (snow water equivalent), the amount of energy H_i in the layer in joules per square meters, and the thickness of the layer ΔZ_i in meters. The layers exchange fluxes of energy and water. The liquid water always moves downward from upper to lower layers. The amount of liquid water cannot exceed the water-holding capacity of the layer [5.5% of the mass of dry snow (Lynch-Stieglitz 1994)]. All the water in excess of that amount is instantaneously moved to the lower layer where it can stay as a liquid, refreeze, or move farther down until it drains out of the snowpack into the soil. We assume that only the fraction of snow above the canopy interacts with the atmosphere while the rest of the snow exchanges the fluxes with the canopy.

Each GCM cell is subdivided into two parts corresponding to bare and vegetated soil. Each part has its own set of prognostic variables and may have a certain fraction of it covered by snow. At each time step the fluxes of heat (W m^{-2}) and water ($\text{m s}^{-1} \text{m}^{-2}$) are computed at the top of each distinct type of surface. Then these fluxes multiplied by corresponding fractions are applied first at the top of the snowpack and together with the fluxes from the snowpack they are used as boundary conditions for the soil routines. A flux limiting technique is applied when computing water fluxes

between the soil layers to ensure that the amount of water in the layer never exceeds the saturation limit and never falls below minimal holding capacity of the layer (Rosenzweig and Abramopoulos 1997).

Surface runoff is calculated based on saturation and on infiltration capacity of the upper soil layer. The underground runoff is computed according to formulation of Abramopoulos et al. (1988), which takes into account the average slope and the density of underground sinks in the cell. A sensitivity test using a new formulation based on a modified TOPMODEL approach (Beven and Kirkby 1979), which uses the statistical characteristics of the local topography (the topographic index), showed an increase in surface runoff compared to underground runoff, but otherwise results were little changed.

2) VEGETATION

Vegetation is divided into 10 different vegetation types with different spectral and masking depth properties, and an explicit dependence of vegetation spectral albedos on leaf area index and solar zenith angle dependence.

A new vegetation canopy conductance scheme has been incorporated into the land surface model as part of an ongoing effort to introduce full vegetation dynamics. The biophysics include vegetation responses to vapor pressure and carbon dioxide concentration, which are known important controls on plant stomatal conductance (Farquhar and Sharkey 1982). This scheme replaces that of Rosenzweig and Abramopoulos (1997) used in SI2000 and is fully documented in Friend and Kiang (2005). The new canopy conductance is a coupled conductance/photosynthesis model that simulates vegetation stomatal control of both transpiration and uptake of CO_2 , within the context of the vegetation type classifications and characteristics of the existing land surface scheme. This model has been developed specifically for use within GCMs to eliminate the computational burden of prior leaf-to-canopy scaling schemes [e.g., the Simple Biosphere Model version 2 (SiB2) of Sellers et al. (1996)] and to incorporate biological variables, particularly leaf nitrogen, that will be linked later to coupled carbon and nitrogen cycles.

The new conductance scheme is responsive to the maximum carbon assimilation capacity, A_{max} ($\mu\text{mol CO}_2 \text{ m}^{-2} \text{ s}^{-1}$) driven by light, canopy temperature T_{can} (K), and leaf nitrogen content N (g N m^{-2} ; Kull and Kruijt 1998); the prognostic internal leaf CO_2 concentration C_i ($\text{mol CO}_2 \text{ m}^{-3}$); the vapor pressure deficit in terms of the foliage interior to foliage surface water vapor mixing ratio gradient, δq_s (kg kg^{-1}); the canopy height h (m) as it affects hydrostatic resistance; and soil

moisture stress β_D as in the Rosenzweig and Abramopoulos (1997) scheme. We define the canopy conductance of water vapor, g_{can} (m s^{-1}), as

$$g_{\text{can}} = \alpha \beta_D (1 - 0.0075h) A_{\text{max}}(\text{light}, T_{\text{can}}, N, n_{f,\text{PFT}}) \times \frac{C_i + 0.004}{5C_i} 2.8^{-80\delta q_s}, \quad (4)$$

where $\alpha = 1.1$ is the eddy-flux-calibrated conductance parameter and $n_{f,\text{PFT}}$ is the plant functional type proportionality factor for capacities of electron transport and Rubisco catalysis per unit leaf nitrogen, derived from fits to eddy flux data for specific plant functional types (PFTs). The canopy radiative transfer scheme distinguishes sunlit versus shaded foliage to take into account the strong impact of diffuse versus direct radiation on total photosynthesis (Gu et al. 2003).

With the introduction of this new conductance scheme to the GCM, regional surface temperatures show a significant improvement (Friend and Kiang 2005). The new scheme also provides an estimate of global primary production (GPP; total uptake of carbon by plant leaves) of 121 Pg C yr^{-1} at preindustrial CO_2 concentrations (290 ppm), which compares well with other estimates ($90\text{--}130 \text{ Pg C yr}^{-1}$) (Cramer et al. 1999; Schlesinger 1991; E. Matthews 2004, personal communication).

k. Lakes

Over land there is a (currently fixed) lake fraction that can be variably ice covered. The lakes are represented with a two-layer energy and mass conserving scheme. The upper layer (minimum depth: 1 m) is assumed to be well mixed, and surface and underground runoff, precipitation, and downstream flow only interact with this layer. The second layer can be arbitrarily deep and exchanges heat, mass, and tracers with the upper layer through mixing driven by wind stirring and convection. The vertical mixing coefficient is $10^{-5} \text{ m}^2 \text{ s}^{-1}$ and is linearly reduced as a function of ice coverage (Liston and Hall 1995). Lakes are assumed fresh and so have a density maximum at around 4°C . Convective overturning of the lake occurs whenever the density in the upper layer exceeds that of the lower layer. In deep lakes (that do not completely freeze up over winter), the lower lake temperature thus reaches a minimum of 4°C . Ice-covered lakes are allowed to completely freeze over (i.e., there is no minimum lead fraction). Solar radiation can penetrate to the second layer based on an extinction coefficient of 2.86 m^{-1} . No geothermal heat flux is prescribed. This scheme replaces a prescription of climatologically fixed temperatures and ice concentration.

If the lake rises above its sill depth, a fraction of the

excess mass (and associated energy) is moved downstream according to a river direction file (Miller et al. 1994; Russell et al. 1995) at a rate dependent on the local topography. River directions are based on the observed predominant routes for water out of any particular grid box but do not take into account the mean topography within a box (i.e., rivers can appear to locally move uphill). If the downstream box contains a lake, then the river flow is added to the upper layer of that lake; if not, the flow is simply saved to be moved farther downstream at the next time step. If a river direction points to an ocean box, the flow is passed into that ocean box. Only if there is a nonzero lake fraction do rivers interact with the atmosphere.

If a lake becomes overdepleted, limits are placed on the evaporation of water and ice formation allowed in order to maintain an absolute minimum lake depth of 40 cm. Lakes at this minimum depth should contract in area, but this is not yet implemented. To prevent such lakes from overheating (since evaporative cooling is restricted) we adjust the lake albedo slightly to match that of the surrounding bare soil so that the amount of absorbed solar radiation is reduced as if the lake had contracted.

There is a small accumulation of water (mainly as snow) over land and in lakes with no outlet to the ocean (e.g., the Caspian Sea). This can amount to 3 mm yr^{-1} globally. For coupled models that need to close the freshwater budget, we allow the river runoff being passed into the ocean to be multiplied by a constant factor (1.05) that is sufficient to ensure zero net loss of water. Further improvements to the lakes scheme (allowing for horizontal lake expansion for instance) and adjustments to the river routing may be able to reduce this bias in the future.

l. Sea and lake ice

Sea and lake ice processes are considered together, although obviously there are some differences [specifically, lake ice is fresh, not advected, and the turbulent heat and mass flux at the base of the ice is more simply parameterized than for (saline) sea ice]. However, surface fluxes (including penetrating solar radiation) and albedo parameterizations are the same. Over the ocean there are salinity effects in the freezing temperature calculations (Fofonoff and Millard 1983) and a salt budget within the sea ice. At present, salt is treated as a passive tracer (i.e., it does not have any thermodynamic role in setting the brine pocket fraction), although future model versions will adopt the formulation of Bitz and Lipscomb (1999).

The sea ice consists of four variable thickness (but fixed fractional height) layers, with each layer having a

prognostic mass, enthalpy, and salt content (Russell et al. 2000). Ice forms with a minimum thickness of 10 cm. After each ice calculation, the layers are renormalized to maintain the fixed percentages of the ice and snow thickness. This technique avoids the problem of disappearing layers in the interior due to internal melting.

Surface ice–atmosphere fluxes follow standard bulk formula flux calculations while basal ice–ocean fluxes are calculated using a viscous boundary layer formulation assuming turbulent heat and salt fluxes between the mixed layer ocean and ice–ocean interface (McPhee et al. 1987). The boundary salinity then sets the freezing point for the interface (Holland and Jenkins 1999; Schmidt et al. 2004). Solar radiation can penetrate the snow and ice and cause internal heating (Ebert et al. 1995). The lateral ice–ocean fluxes follow the detailed descriptions in Schmidt et al. (2004) and are based on modified formulations of Briegleb et al. (2002). The snow density and thermal conductance are assumed to be 300 kg m^{-3} and $0.35 \text{ W m}^{-1} \text{ K}^{-1}$, respectively. For ice the values are 916.6 kg m^{-3} and $2.18 \text{ W m}^{-1} \text{ K}^{-1}$. In the event that snow causes the snow–ice line to be pushed below the equilibrium water line, snow–ice is formed that can incorporate as much seawater as the energy available for freezing within the snow will allow (Schmidt et al. 2004). This occurs predominantly in Antarctic waters.

The sea ice dynamics are based on a recent formulation of the standard Hibler viscous-plastic rheology (Zhang and Rothrock 2000). This component is calculated on the atmospheric grid in order to have consistency across different ocean model resolutions. This does not allow us to take maximum advantage of the available resolution of ocean surface currents, though this restriction will be removed in future versions.

In a control run with specified monthly varying SST and sea ice extent, the sea ice thickness is prescribed to be locally proportional to the extent (in lieu of a good climatology). The constant of proportionality is dependent on hemisphere and the number of months with observed ice cover. Maximum thickness in the Northern (Southern) Hemisphere is 3.5 m (2 m), in line with observations. There are no explicit lateral fluxes in this case, and the calculation of the basal heat flux is simplified. The advective fluxes of sea ice are driven primarily by atmospheric winds and can be calculated (assuming no ocean currents) in order to estimate the horizontal ice mass and energy convergence needed for the q -flux calculation (see section 3o below).

m. Land ice

Land ice is treated as in previous models, and as in SI2000, broadband albedos over the Greenland and

Antarctica ice sheets are fixed at 80%. Glacial runoff related to calving icebergs and under-ice-sheet cavity melt is added to the ocean (as ice) around Antarctica and Greenland. Snow accumulation is $2016 \times 10^{12} \text{ kg yr}^{-1}$ in Antarctica and $316 \times 10^{12} \text{ kg yr}^{-1}$ in Greenland based on IPCC estimates (Houghton et al. 2001). However, accumulation in the model is somewhat higher, around 4032 and $948 \times 10^{12} \text{ kg yr}^{-1}$ in each hemisphere. We therefore choose to add this amount to the ocean in order to balance the mass budget of the major ice sheets. This does not impact the atmosphere-only runs, but it does affect the implied ocean heat transports and any prognostic ocean model [including runs with ocean thermodynamics (see below)]. Since this is a constant addition, imbalances may arise as a function of climate change.

n. Ocean, lake, ice, and land surface coupling

The results of model runs with dynamic oceans will be discussed elsewhere (A. Romanou et al. 2005, unpublished manuscript), but we briefly describe here the coupling procedure used for all ocean models. ModelE has been coded so that synchronous coupling at the frequency of the physics time step (30 min) is possible, but an ocean model is not forced to take advantage of that. Coupling is always by fluxes of the fundamentally conserved quantities (mass and energy). Thus even though specific modules may make certain assumptions (such as volume rather than mass conservation in the ocean), the coupling does not make any such assumption. For instance, the basal fluxes of energy, freshwater mass, and salt mass at the ice–ocean interface are specified separately, rather than having the ice model assume how the ocean will deal with them.

At the beginning of the flux calculation, we calculate the lateral melt for the sea/lake ice. This ensures that the ice fraction can be kept constant over all the subsequent flux calculations. Given the surface conditions, the atmospheric model calculates the precipitation, radiative, and other surface fluxes (surface wind stress, evaporation, and sensible and latent heat) over each surface type. These fluxes are first applied directly to the land surface (soils, vegetated ground, and glaciers). Using the atmosphere–ice wind stress, the sea ice dynamics calculates the horizontal ice velocities and the resulting ice–ocean stress. Given the ice–ocean stress (and hence the effective interface friction velocity), we can then calculate the heat, salt, and mass fluxes at the ice–ocean interface (Schmidt et al. 2004). The thermodynamic sea/lake ice model then uses the basal and surface fluxes to update the column ice variables.

Runoff from the land surface and glacial melting is passed to the lake routines, along with the atmosphere–

lake and ice–lake basal and lateral fluxes. The lake module decides whether there is any outflow into a downstream river. The river outflow and the (fixed) iceberg calving flux, combined with the atmosphere–ocean and ice–ocean fluxes, are then passed to the ocean module. Both the lake and ocean modules can decide to create frazil ice if the surface fluxes would cool water to the freezing point (which is a function of salinity in the ocean). These fluxes are calculated separately below existing ice and in open water so that the additional ice can add either to the thickness or to the extent consistently. We then make an additional call to the sea ice module so that (i) the newly formed ice can be added to the ice variables, and (ii) that ice can be advected according to the ice velocity field calculated earlier.

The multistage call to the ice modules allows us to ensure that the sea ice fraction is consistent for the all flux calculations, and that the advection of ice does not create or remove ice for which other fluxes had been calculated (but not yet applied). This does complicate the interface with a generic ice model, but the advantages of physical consistency are hopefully clear.

o. q -flux ocean

Atmospheric models are often run with simplified thermodynamic ocean models that allow the SST to adjust to different atmospheric fluxes but that hold the ocean heat transports constant, for instance, in order to estimate climate sensitivity (Hansen et al. 1984; Russell et al. 1985). The basis for the calculation of the ocean heat convergence (the q fluxes) is that, given the knowledge of the heat and mass fluxes at the base of the atmosphere, the lateral fluxes from sea ice advection (both derived from a control run with specified SST and ice extent as described above) and knowledge of the observed mixed layer temperature and depth, the oceanic heat convergence into the mixed layer (assumed isothermal) can be calculated as a residual. While straightforward in conception, the details of this calculation can be problematic. To avoid problems in estimating the ice–ocean flux in situations where the ocean is not varying, we consider the whole mixed layer plus sea ice plus snow mass as our control mass. It is important that the control run is close (within 0.5 W m^{-2}) to energy balance at the surface (or equivalently at the TOA), otherwise a drift will ensue when using the calculated q fluxes.

The daily accumulated fluxes of absorbed solar radiation, net LW radiation, and latent and sensible heat over the ice and ocean fractions are saved. In addition, the gridbox mean (latent) energy of precipitation and energy of river/glacial runoff (which is distributed over

both the ice-covered and open-ocean fractions) are also saved. If ice dynamics are being used, we also accumulate the net ice energy convergence due to the calculated horizontal ice tendencies. At noon each day we save the total ice and snow mass and total energy of the sea ice. A 5- or 10-yr climatology for these fluxes is generally sufficient.

The global annual mean sum of the saved fluxes should be close to zero if the control run was close to radiative balance. Any remaining imbalance is corrected for, so that the global annual mean q flux is absolutely zero. This is a small correction and does not noticeably affect the subsequent q -flux run.

The structure of the q -flux ocean consists of two layers: a mixed layer (assumed isothermal) of monthly varying depth fixed by observations and a second layer that covers the depth between the base of the current mixed layer and the depth of the maximum (winter) mixed layer. The temperature at the base of the maximum mixed layer is set as the temperature of the mixed layer at the time of maximum depth and is unchanged until the mixed layer next reaches that level. The second-layer temperature is set to conserve energy as the mixed layer entrains or detrains mass. Given the specified SST and sea ice fraction in the control run, the field of monthly varying ocean mixed layer depths, and the mass, energy content, and snow cover of the sea ice, the temperature structure and energy content of the q -flux ocean are defined over the control mean annual cycle.

We expand the vertical fluxes and the total energy content for each grid box in a Fourier series and retain only the first five harmonics. This captures the bulk of the temporal variability without introducing too much insignificant noise. We define the q flux as the difference between the rate of change of the energy content and the incoming flux for each spectral component. Since the rate of change integrated over a year is by definition zero, the mean q flux in a box is simply minus the integrated vertical flux. No further adjustments to the q fluxes are made at the gridbox level.

We note that, by design, the fluxes provided by this procedure not only incorporate both the actual ocean heat fluxes but also all surface flux energy errors implied by the model physics. For instance, an error in cloud cover that leads to excessive incident solar radiation at the surface will at least be partially balanced by increased implied downward flux at the base of the mixed layer.

When used prognostically, the q fluxes are added to the mixed layer at each time step. Surface fluxes are applied separately to the open-ocean and ice-covered fractions in order to separately estimate changes in ice thickness and extent. Occasionally, ice thicknesses can

exceed the amount of mass assumed in the mixed layer calculation, and in such cases the excess ice is removed (while keeping temperature constant). This is an additional small leak of energy and freshwater but is not significant in the global budget for reasonable climate changes. We note that the q -flux version of ModelE is energetically stable if started from initial conditions corresponding to the end of the relevant specified SST run. This is unlike some previous versions that were affected by a number of small inconsistencies and energy losses, which led to a drift in the q -flux climate.

In transient runs, we optionally include a purely diffusive 12-layer-deep ocean (to 5000 m). This module diffuses down the anomalies of temperature at the base of the mixed layer using diffusion coefficients derived from ocean tritium studies (Hansen et al. 1984).

4. Tracers

Passive tracers are an intrinsic part of the model and are controlled by a combination of preprocessing directives for classes of tracer, and logical switches for various tracer-specific processes. Gas phase tracers, soluble tracers (including tracers of water mass such as isotopes, age, or source region), and particulate tracers are incorporated. All resolved mass fluxes (in the advection, moist convection, etc.) affect tracers, and all hydrologic processes are followed completely for any soluble or intrinsically water-based tracers. Large-scale advection (and subsidence within the moist convection scheme) is performed using QUS. Surface concentrations and fluxes are determined using the same code as described above for heat and humidity, but with appropriate tracer-specific bottom boundary conditions (including turbulent dry deposition, gravitational settling, and interactive sources). Detailed results for individual groups of tracers (including tropospheric and stratospheric chemistry, mineral dust, sulfate, nitrate and carbonaceous aerosols, cosmogenic tracers, gas phase tracers, and water isotopes) will be reported elsewhere.

Compared to previous descriptions of GISS GCM tracer physics (Koch et al. 1999, 1996; Rind and Lerner 1996; Rind et al. 1999; Shindell et al. 2001; etc.), the tracers in ModelE are much more consistent with the base model physics, particularly near the surface. In the clouds, a prognostic cloud water tracer budget is included (for soluble tracers), and the moist convection routine has been adapted to be locally and globally tracer mass conserving. Multilevel tracer budgets in sea ice, soils, lakes, and rivers are also now included if required. Aerosol and trace gas interactions with the radiation scheme are now much more straightforward.

5. Evaluation

We endeavor to compare the model simulations to as many suitable datasets as possible. Since we are interested predominantly in global climate, the wide coverage obtained with satellite remote sensing is crucial. However, satellite views of the world must be treated with caution if sensible comparisons are to be made. For instance, the vertical weightings implicit in the Microwave Sounding Unit (MSU) datasets (Fu et al. 2004; Hansen et al. 2002) must be matched in the model diagnostics (Shah and Rind 1995). Similarly, satellites that see clouds cannot generally see through them, and this needs also to be accounted for [see below for details of the ISCCP simulator (Klein and Jakob 1999; Webb et al. 2001)]. Where useful gridded datasets exist of selected in situ data we use those. Similarly, high-level products from the reanalysis projects [particularly the European Centre for Medium-Range Weather Forecasts (ECMWF) 40-yr Re-Analysis (ERA-40; Simmons and Gibson 2000)] will be used where no other climatological data exist. The fields discussed in the following section are taken from 10-yr means of the circa 1979 climatological simulations. They provide an inevitably incomplete view of the model climatology; however, they do outline the principal successes and continuing problems with the models. The various data products are from differing periods, but changes over time are small compared to the differences seen.

The global mean quantities described in Table 3 show that some elements of the simulations are remarkably robust to resolution and further improvements to the stratosphere. The net albedo and TOA radiation balance are to some extent tuned for, and so it should be no surprise that they are similar across models and to observations. Precipitation is uniformly high (compared to the Global Precipitation Climatology Project (GPCP)/Climate Prediction Center (CPC) Merged Analysis of Precipitation (CMAP)), but this might partially reflect undercounting in the remote sensing. The global Bowen ratio (sensible heat/latent heat) $\approx 25\%$ is systematically small compared to canonical estimates $\approx 30\%$ (Kiehl and Trenberth 1997), but larger than that seen in another recent model [i.e., AM2/LM2 Geophysical Fluid Dynamics Laboratory (GFDL) model $\approx 22\%$ (GFDL Global Atmospheric Model Development Team 2004)]. Total cloud cover is definitely too low.

a. Radiation data

Estimates of the TOA radiation balance from the Earth Radiation Budget Experiment (ERBE, 1985–89; Harrison et al. 1990) are compared to the models in

TABLE 3. Global annual mean model features and key diagnostics compared to observations or best estimates.

Field	M20	F20	M23	Obs
SAT (°C)	14.4	14.5	14.3	14.0 ^a
Planetary albedo	29.7	29.6	29.3	30 ^b /29.5 ^c
Cloud cover (%)	58.4	56.9	58.8	69 ^d
Precipitation (mm day ⁻¹)	2.96	2.99	3.01	2.67 ^e /2.65 ^f
Atm water (mm)	25.0	25.1	24.7	24.5 ^g
Energy fluxes (W m ⁻²)				
TOA absorbed SW	240.3	240.8	241.5	239.3 ^b
TOA outgoing LW	240.1	240.6	241.4	234.5 ^b
TOA SW cloud forcing	-46.3	-46.2	-45.6	-48.4 ^b
TOA LW cloud forcing	22.5	23.1	21.1	31.1 ^b
Surface absorbed SW	168.0	168.6	169.4	165.2 ^h
Surface net LW	-60.5	-61.2	-60.2	-50.9 ^h
Sensible heat flux	20.9	19.7	21.5	24i
Latent heat flux	85.6	86.6	86.7	78 ⁱ
Tropical lower-stratosphere water vapor minima (ppmv)	3.3	3.8	2.7	3.8 ± 0.3 ^j
Zonal mean tropopause temperature (min, Jan) (°C)	-80	-78	-82	-80
Hadley circulation (Jan) (10 ⁹ kg s ⁻¹)	179	170	180	175–200 ^k

^a Jones et al. (1999).^b ERBE (Harrison et al. 1990).^c Palle et al. (2003).^d ISCCP (Rossow and Schiffer 1999).^e CMAP (Xie and Arkin 1997).^f GPCP (Huffman et al. 1997).^g NVAP (Randel et al. 1996).^h Zhang et al. (2004).ⁱ Kiehl and Trenberth (1997).^j Dessler (1998).^k Waliser et al. (1999).

Figs. 3 and 4. The patterns in each model configuration are similar to each other and to the observations. There is a hemispheric bias due to excessive absorption in the southern oceans, which is compensated for by a similar deficit in the north. There is excessive absorption off eastern South America and Africa—mainly due to a deficit of low marine stratocumulus decks. The higher-resolution model F20 does match the equatorial patterns over Africa and the eastern Pacific better than the coarser-resolution models.

Comparisons to MSU 1978–2004 brightness temperature climatologies (Mears et al. 2003) reveal slightly different biases in each model configuration (Figs. 5 and 6). We highlight results from channels 2 and 4, which have global weightings centered on 600 and 70 hPa, respectively (though with substantial tails). We calculate the brightness temperatures in the model using a radiative transfer calculation that takes into account surface emissivity, atmospheric water vapor, and temperature profiles (Shah and Rind 1995). While interannual anomalies are similar with this approach to using static weighting functions, the absolute values compare slightly better to observations, particularly in high-latitude regions. We show here the anomalies with

respect to the observations of the annual mean of the monthly climatologies. For MSU-2, all models show good general agreement with the observations but have a similar continental warm bias (possibly due to a too-simple assumption of constant land surface emissivity of 1.0 in the absence of snow). M20 and M23 have slight cool biases in the high latitudes (<2°C). F20 has less of a bias in the high latitudes (with the exception of Antarctica), but has a small warm bias over the tropical oceans. For MSU-4, midlatitudes are generally cool, although notably better in M23. Again, Antarctic values are less well simulated, particularly in F20.

b. Cloud-related data

ISCCP has produced datasets of cloud properties and distribution (Rossow and Schiffer 1999; D2, 1983–2001) that can be used for model evaluation. In addition, Klein and Jakob (1999) and Webb et al. (2001) have produced an ISCCP simulator that can be applied to the model variables in order to give a “satellite’s-eye” view of the model. In this way, some of the characteristics of the measurements can be incorporated directly

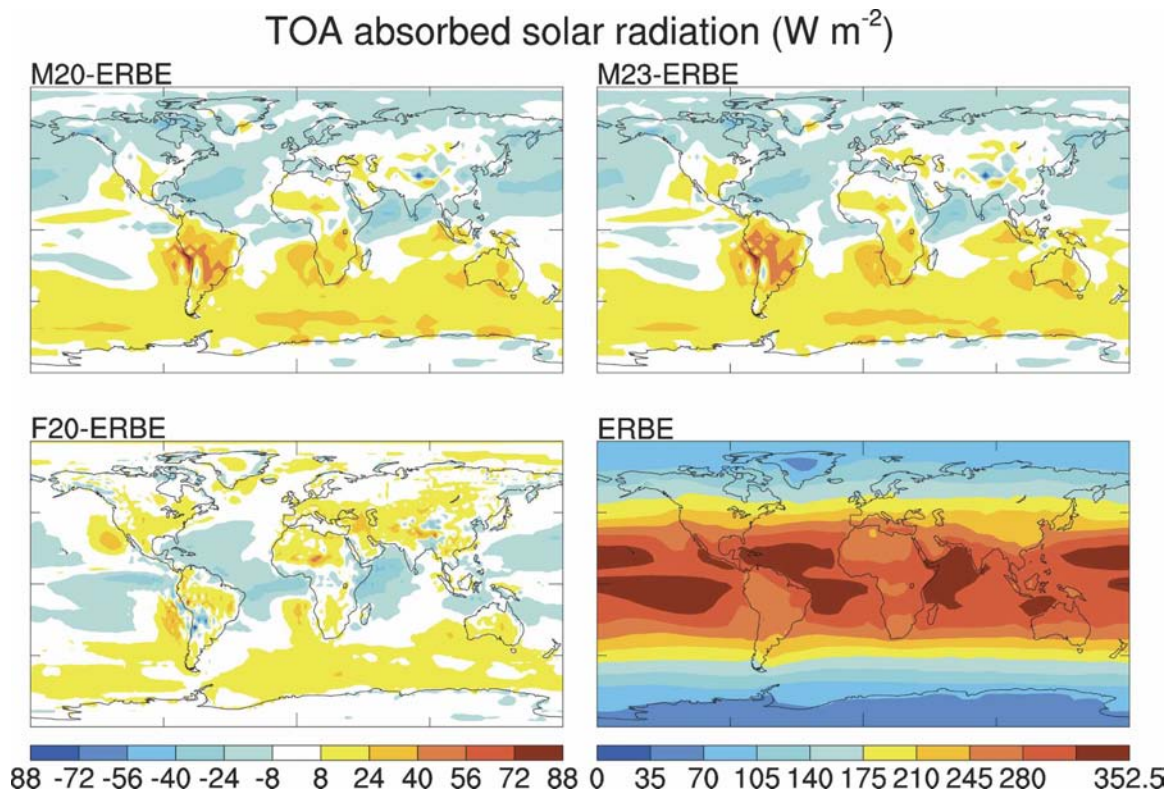


FIG. 3. TOA annual mean absorbed solar radiation anomalies from ERBE.

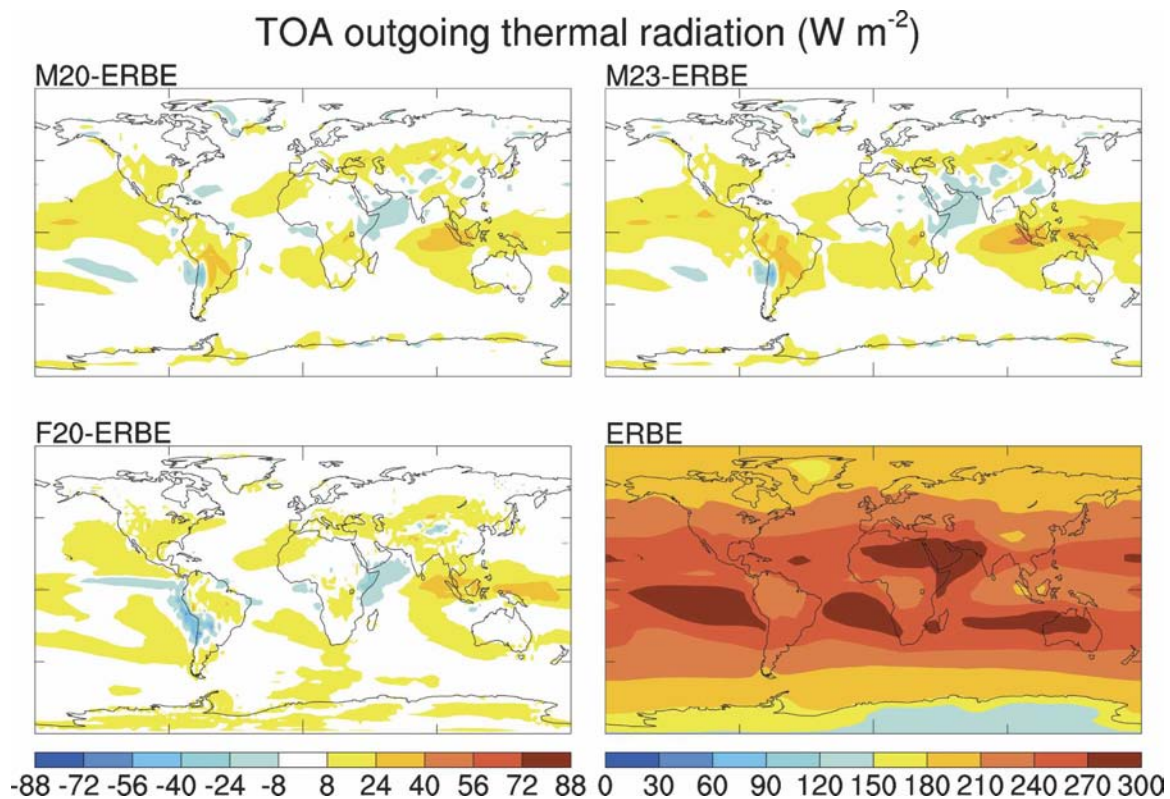


FIG. 4. TOA annual mean outgoing thermal radiation anomalies from ERBE.

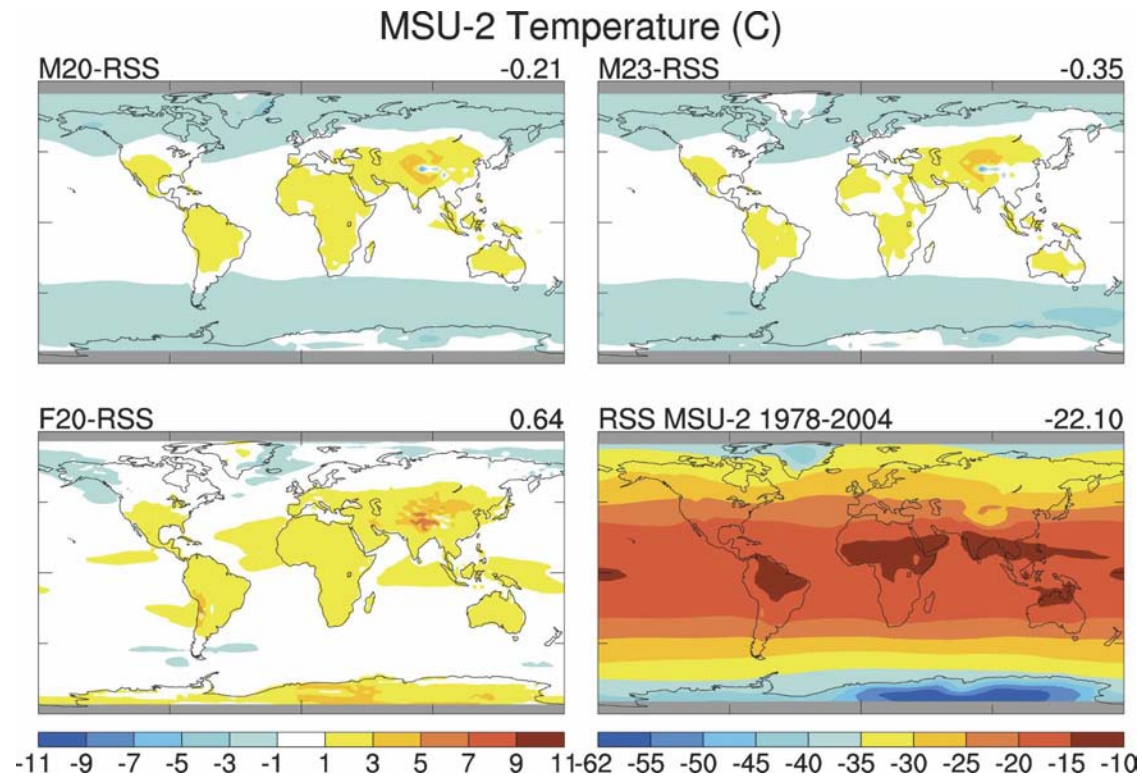


FIG. 5. MSU-2 (midtroposphere) annual mean temperature anomalies with respect to the RSS climatology. GCM diagnostics use a radiative transfer calculation to calculate the brightness temperature.

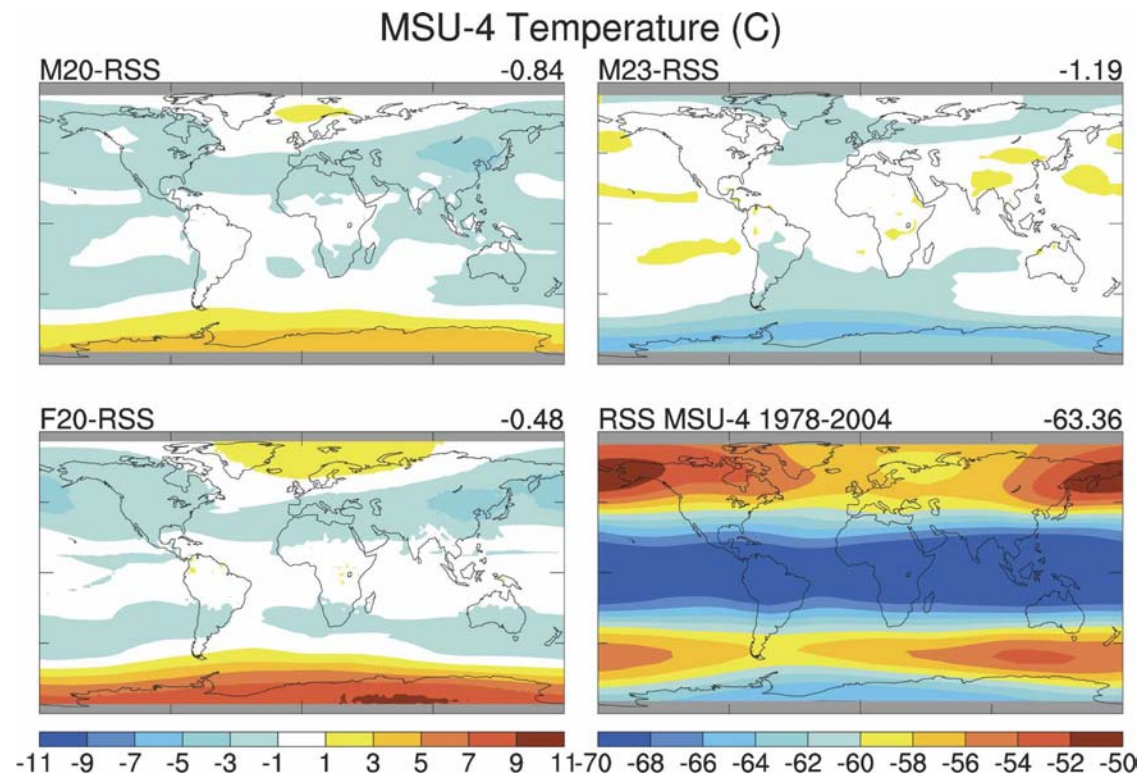


FIG. 6. MSU-4 (stratospheric) annual mean temperature anomalies.

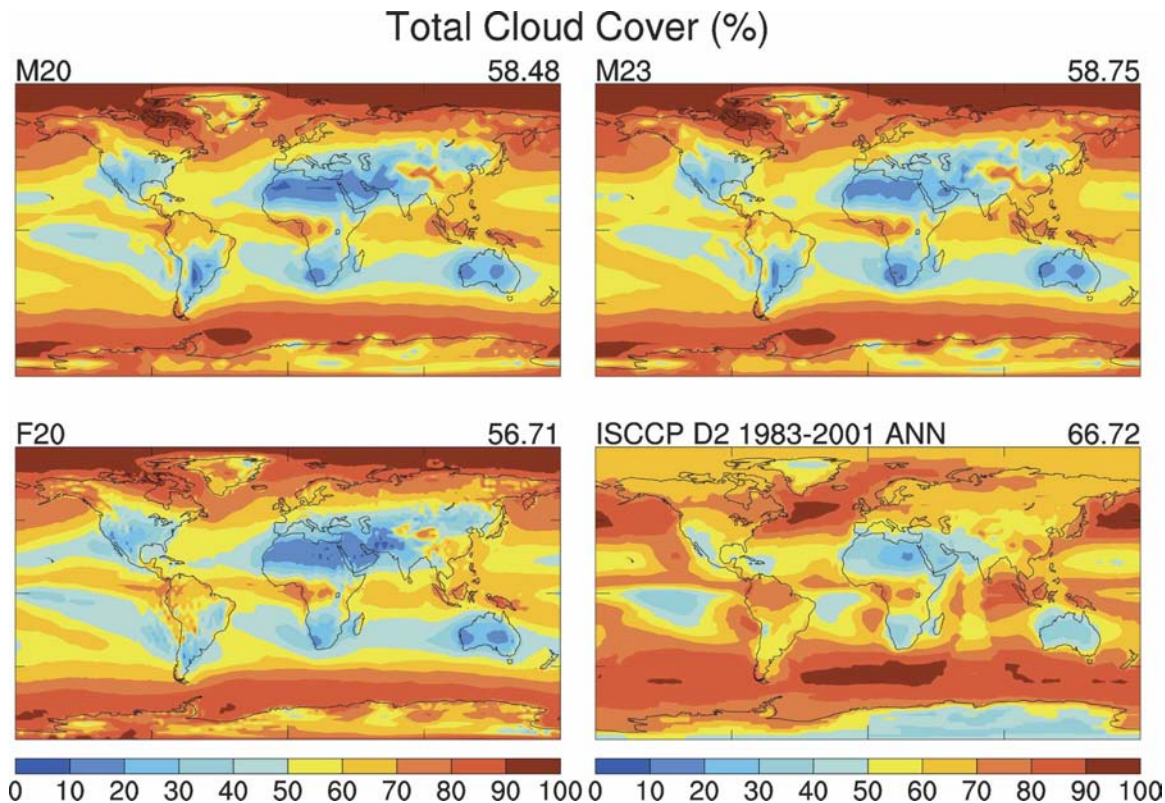


FIG. 7. Annual mean total cloud cover (%) compared to ISCCP.

into the diagnostics and thus provide a cleaner comparison. We look at three key diagnostics of the model cloud fields. First, the total cloud amount (Fig. 7) is systematically too low in these model runs. Since planetary albedo (Fig. 3) is reasonable, this implies that cloud optical depths must be too high.

Second, the cloud-top pressure as calculated by the ISCCP algorithm (Fig. 8) is systematically too low (by about 100 hPa). The actual cloud tops (i.e., the level of the highest cloud layer in the model; not shown) are always higher than those calculated by the ISCCP algorithm; however, these are still systematically too low, particularly in the tropical marine stratocumulus regions. Del Genio et al. (2005b) have shown that ISCCP low cloud-top altitudes are biased high compared to cloud radar data, because of input water vapor and temperature profile errors and contamination by overlying thin cirrus. However, the GCM low cloud tops are still somewhat too low compared to the radar results. Equatorial features are again better captured with the higher-resolution model F20, but otherwise the patterns are similar. In the Sahara, low clouds seen in the data are most probably dust cloud contamination and do not reflect a problem with the models.

Third, we examine the ISCCP histograms of annual mean cloud-top pressure/optical depth pairs (Fig. 9). Actual low cloud cover (below 680 hPa) in the models is around 43%–46%, compared to coverage of 27%–29% that is viewable from above (the ISCCP climatology has 26%). The low clouds in the model are, however, at a lower level than seen in ISCCP, peaking at around 900 hPa. There is a tendency to have the higher (ice) clouds be too optically thick (i.e., particle sizes are too small or there is too much ice or the clouds are too physically thick), consistent with the albedo and cloud cover diagnostics mentioned above.

The cloud radiative forcing is again very similar across the models and, in the global mean, similar to the ERBE analysis (Fig. 10). Looking more closely, the models have SW forcing in the Tropics that is too negative, but not negative enough in the midlatitudes. For the LW forcing, model values in the Tropics are too low (by up to 20 W m^{-2}).

c. Implied ocean heat fluxes

By spatially integrating the annual mean ocean heat convergence from the southern boundary, we can derive the implied ocean heat transports. These are a

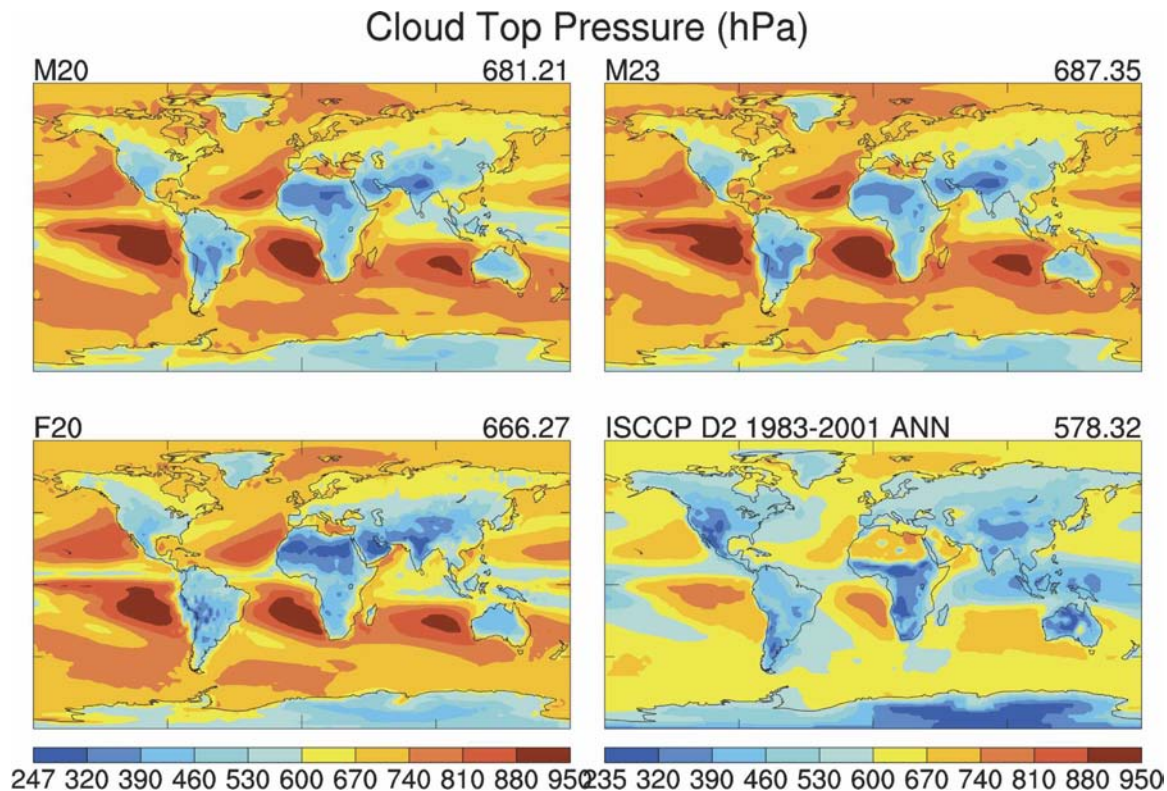


FIG. 8. Annual mean cloud-top pressure (hPa) calculated using the ISCCP simulator compared to ISCCP observations.

function of the atmosphere and sea ice models and should be close to that estimated from observations or provided by a dynamic ocean model if drift in any fully coupled model is to be minimized. For each of the models we compare these implied heat fluxes to various estimates made from in situ observations and inverse models, and from atmospheric budget residuals (Fig. 11). The comparison is reasonable and close to what global ocean models will provide. However, the NH peak is slightly larger than that supplied by our dynamic oceans.

d. Hydrological data

The precipitation patterns (Fig. 12) are closely related to the observed GPCP (1987–98) patterns (Huffman et al. 1997), although the rainfall in the western warm pool is in excess of that observed, while Amazonian rainfall is less. Some improvement is seen in the F20 runs near the equator, but all versions are deficient in north/eastern Eurasia and have excessive precipitation around the Himalayas and in Central America. Changes to the dynamics around steep topography mentioned above did lead to improvements around mountains, but the current results indicate that further work is still needed in this area. Precipitation is also deficient in the NH storm tracks.

The inclusion of a turbulent flux of humidity and tracers throughout the vertical column has greatly improved a long-standing dry bias in the GISS models. Total column water (Table 3) is now much closer to that observed. Comparing the specific (Fig. 13) and relative humidity (not shown) in the troposphere shows that patterns in the models are very similar to that seen in the ERA-40 reanalysis.

Near-surface 850-hPa specific humidity values are well modeled, with slightly high values in the Tropics (Fig. 13), which is also seen in the relative humidity (not shown). Northern Eurasia is particularly dry though, and in the relative humidity field, the Arctic and Southern Ocean regions stand out as being too dry also. Atlantic and Pacific values seem reasonable though. In the upper troposphere (300 hPa), the tropical wet bias is enhanced (in both the relative and specific humidity), and the dry bias in the midlatitudes is more general. Resolution appears to play little role in these differences, the best simulation being given by the M20 model. The ERA-40 (1979–2000) values compare well to the Television Infrared Observation Satellite (TIROS) Operational Vertical Sounder (TOVS) remotely sensed data but are significantly different to the National Centers for Environmental Prediction (NCEP) reanalysis product. Additionally, ModelE per-

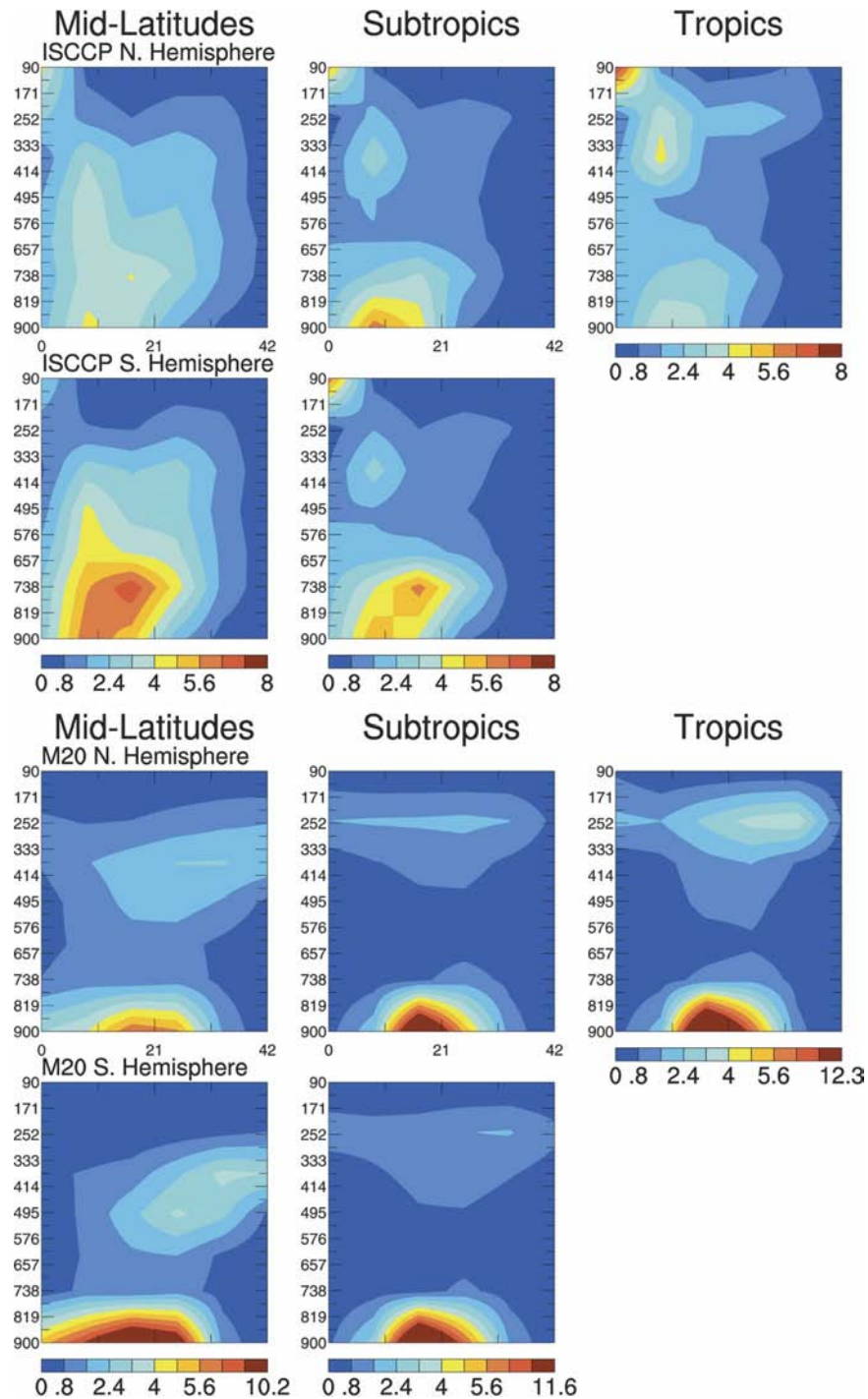


FIG. 9. ISCCP optical depth/cloud-top pressure histograms for different regions (NH mid-latitudes: 60° – 30° N; NH subtropics: 30° – 15° N; Tropics: 15° N– 15° S, etc.). Model output is only shown for M20. Other configurations are similar.

forms quite well relative to TOVS upper-tropospheric humidity (UTH) and National Aeronautics and Space Administration (NASA) Water Vapor Project (NVAP) column water vapor, about as well as ERA-40 and bet-

ter than the NCEP reanalysis (not shown; Bauer and Del Genio 2006).

In the Tropics (12° S to 12° N), the M20 and M23 models show a seasonal cycle and water vapor tape

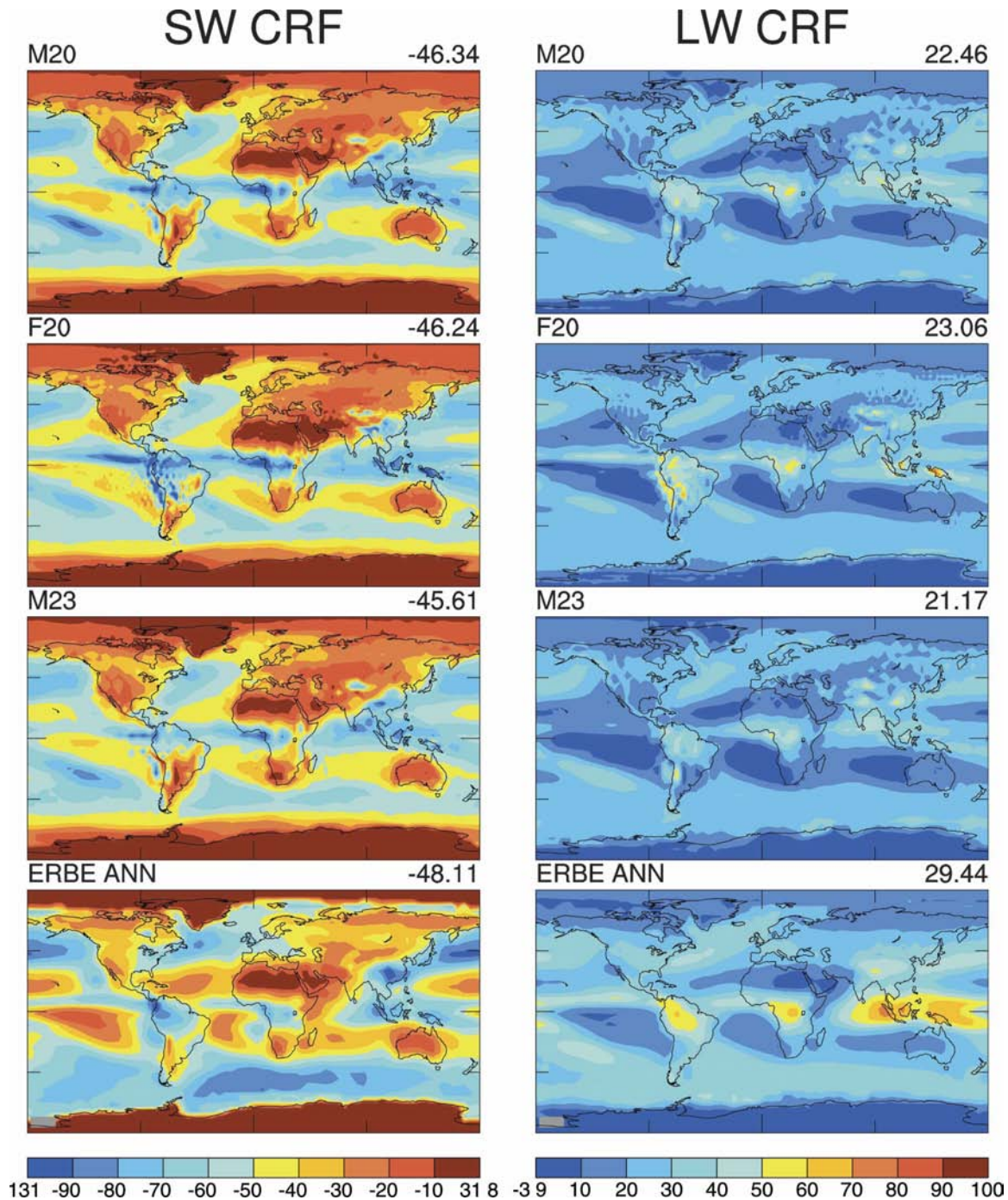


FIG. 10. Cloud radiative forcing calculated within the models and compared to ERBE estimates.

recorder effect similar to that seen in the Halogen Occultation Experiment (HALOE) observations (version 19; 1991–2003; Russell et al. 1993; see Fig. 14). The F20 model is slightly too wet and too warm, and hence has a reduced amplitude variation. We show the relative departures from the mean humidity at each level

since that compensates for the overall differences in lower stratospheric values (Table 3). The rate of vertical ascent of the water vapor anomalies is comparable in all cases, although the midstratospheric semi-annual oscillation in water vapor is clearest in the M23 model.

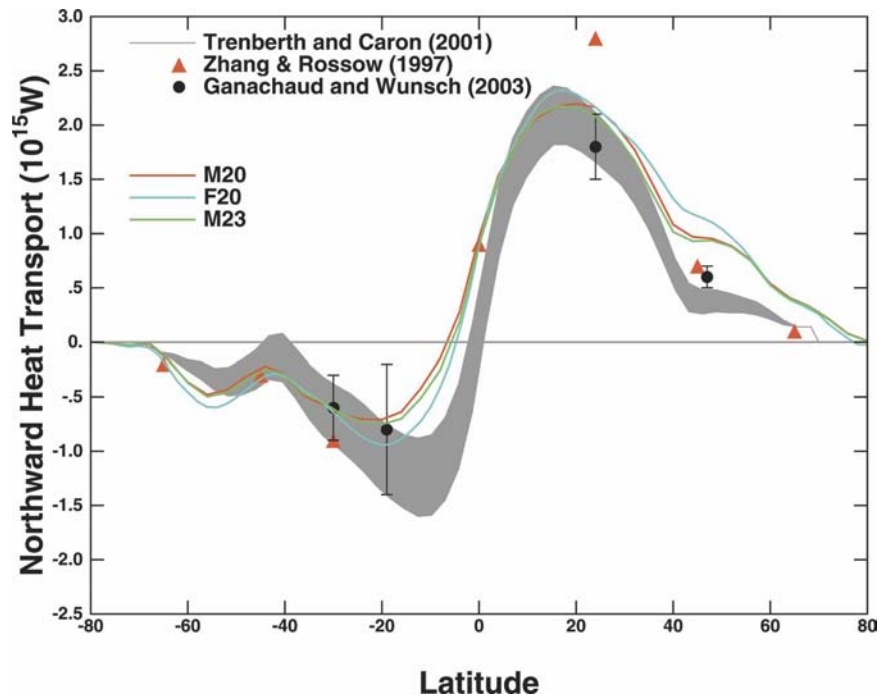


FIG. 11. Implied annual mean poleward ocean heat transports from the integrated q fluxes calculated from the climatological model runs and comparison with residual calculations (with error bars) from the NCEP reanalysis (Trenberth and Caron 2001), from the ISCCP remotely sensed fluxes (Zhang and Rossow 1997), and from ocean inverse calculations (Ganachaud and Wunsch 2003).

e. Zonal mean temperature and wind data

The zonal mean temperature (Fig. 15) and zonal wind (Fig. 16) need to be evaluated up through to the stratopause, and since the reanalysis projects do not go up that high, we use the Cooperative Institute for Research in the Atmosphere (CIARA) dataset (for the period prior to the ozone hole, an appropriate comparison for these runs; Fleming et al. 1990). These diagnostics are shown only for January conditions, but the differences between the resolutions are clear. The M20 model (which goes to the stratopause) does a reasonable job up to the lower stratosphere, but above that, the M23 model does better (due to its inclusion of the GWD scheme and higher model top). In particular, the high-latitude stratopause break in the winter hemisphere, caused by gravity-wave-driven downwelling, is much more clearly seen in M23. The minimum temperatures seen in the lower stratosphere are coldest in M23, then M20, and are relatively warm in F20 (Table 3). The winter polar vortex is slightly too cold in M23 and too warm in M20 and F20. All models exhibit a lower-stratosphere (≈ 200 hPa) cold bias near the summer hemisphere pole ($\approx 10^\circ\text{C}$).

In the zonal mean velocities, M20 again has the best

correspondence to the data up to the lower stratosphere, but above it is too damped, similarly to F20. M23 is better but has the maximum winds at the stratopause too far poleward—a common problem in middle-atmosphere models. Peak winds in the jet streams are slightly high in all cases.

f. Surface data

Surface air temperatures (SATs; Fig. 17) show a general warm continental bias in comparison to the updated Climate Research Unit (CRU) data (Jones et al. 1999). In mid- to high-latitude regions (i.e., eastern Siberia) this is mainly a wintertime phenomenon possibly related to a lack of snow cover, although we note that the bias in the ERA-40 reanalysis is very similar (Betts and Beljaars 2003). Over the Sahara, there is a slight underestimate of the surface albedo, leading to excessive warmth (1° – 3°). Tropical coastal areas appear to be slightly cool. As in the other diagnostics, the differences among the different models are small compared to the offset with observations.

We use the ERA-40 reanalysis products averaged from 1979 to 2000 to compare the sea level pressure (SLP) and wind stress over the ocean (Simmons and

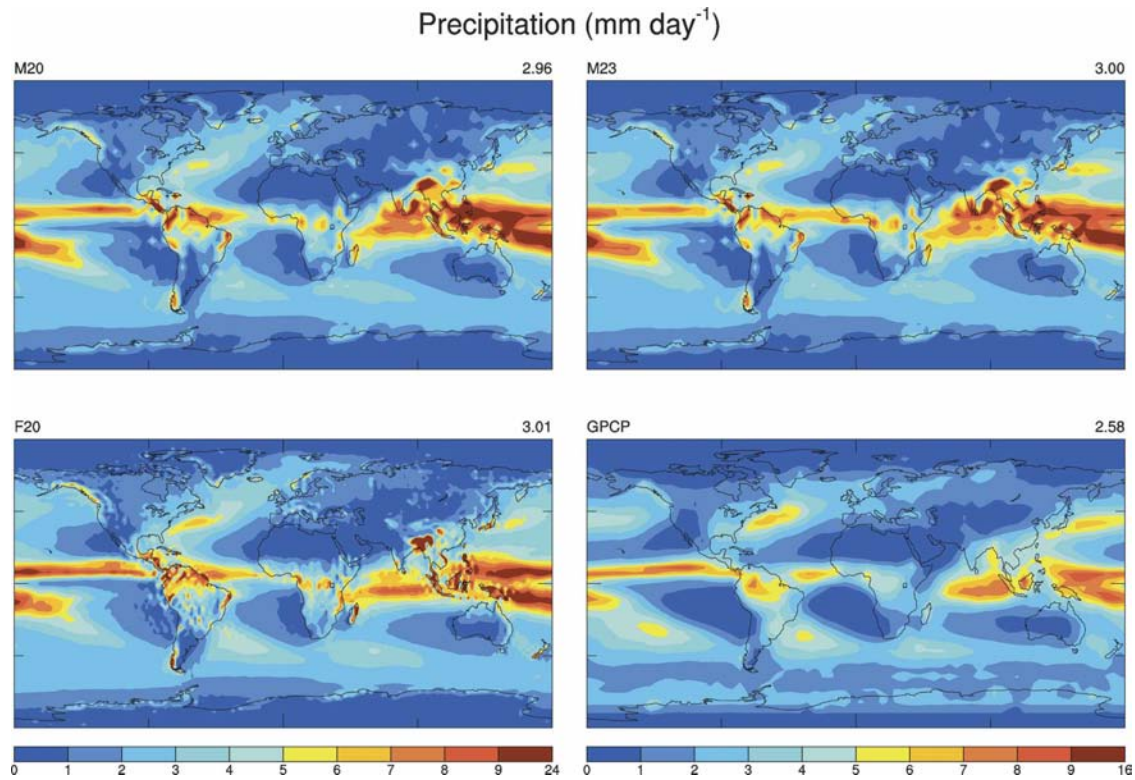


FIG. 12. Annual mean precipitation compared to the GPCP (1987–98).

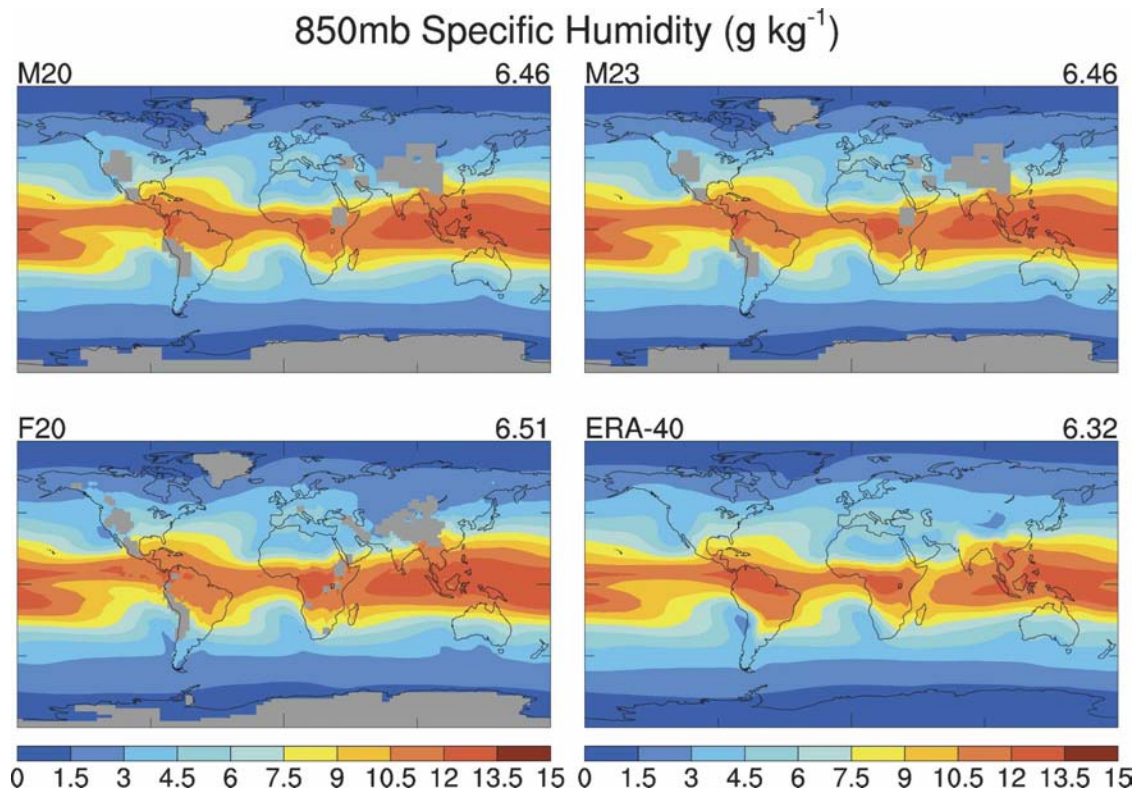


FIG. 13. Comparison of specific humidity at 850 hPa with ERA-40.

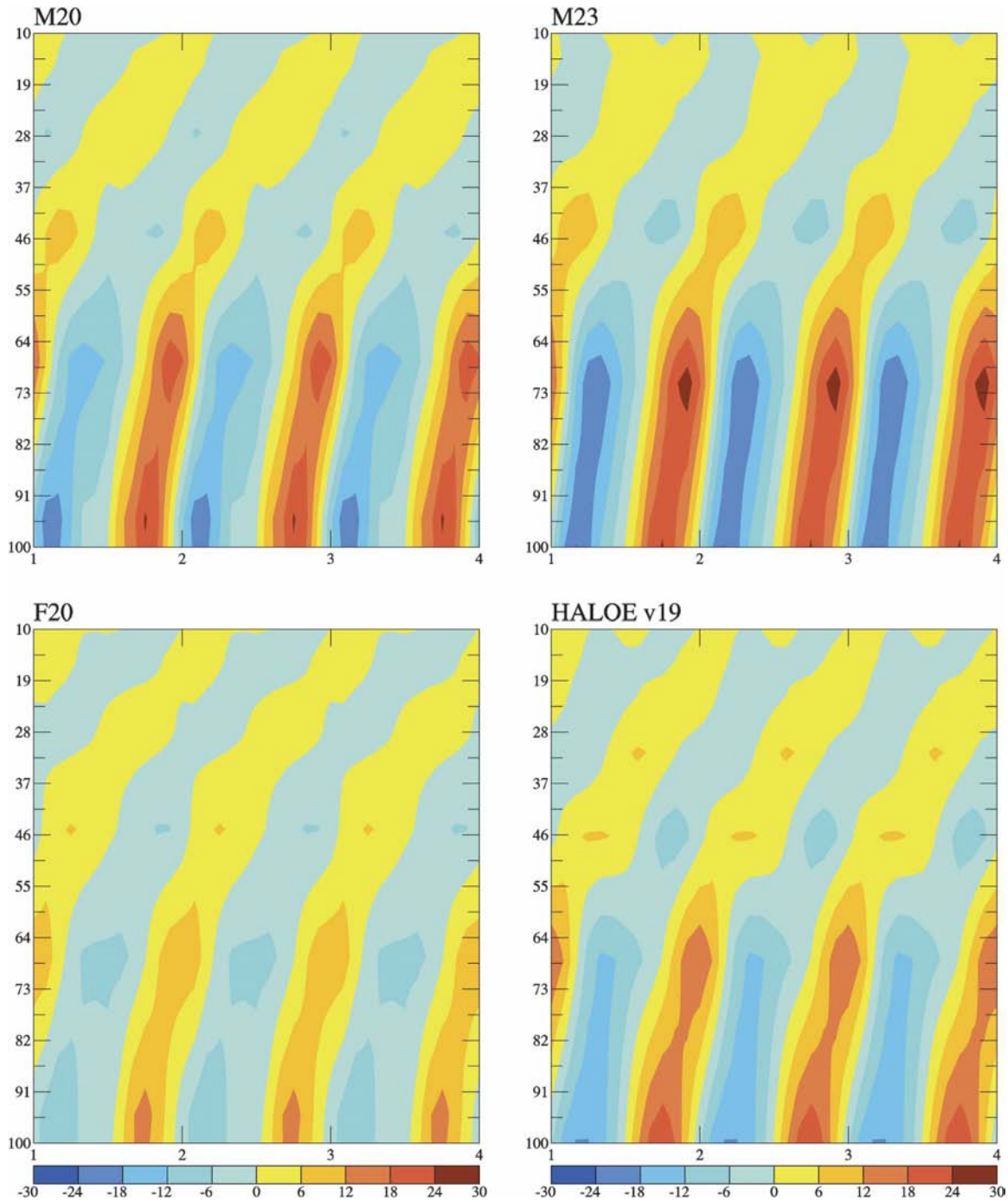


FIG. 14. The percent deviation from the mean in specific humidity compared to the HALOE data in the tropical upper troposphere/lower stratosphere (12°S – 12°N). Each picture is a climatology, repeated 3 times to allow the stratospheric tape recorder effect to be made clearer.

Gibson 2000). All models have too low SLP in the Tropics (Fig. 18). Arctic SLP is too high in the medium-resolution models (M20 and M23) but reasonable in F20. Related to this is the too-weak Icelandic low in the wintertime in M20 and M23, and a better extension into

the northern North Atlantic in F20. The Southern Ocean low pressure areas are not sufficiently low in the simulations, particularly in JJA. We note that changes in the stratospheric drag can have a big impact on SLP with increased drag being associated with higher SLP.

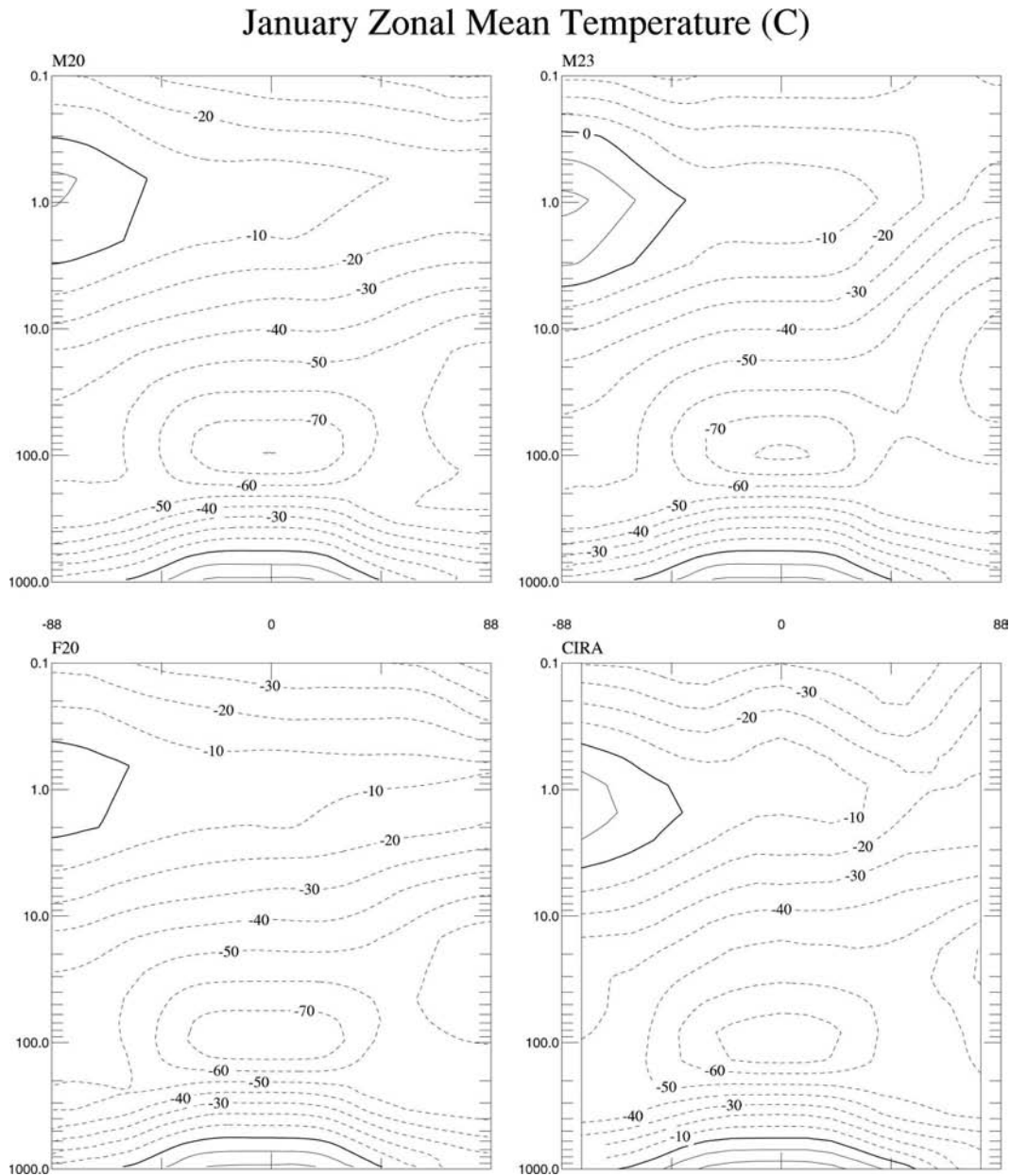


FIG. 15. CIRA climatology and model output for January zonal mean temperature.

The location of NH storm tracks is reasonably well simulated in M20 and M23 (Fig. 19), although the absolute number of storms is low, particularly in the eastern Pacific. This is a location that is an important center for secondary cyclone formation, which is not well simulated at this horizontal resolution (Bauer and Del Genio 2006). The higher-resolution data are somewhat better in this regard (not shown). The wind stress patterns are reasonably well modeled in all configurations (Fig. 20), although the North Atlantic and Southern

Ocean magnitudes are a little low in M20 and M23, consistent with the storm-track results.

g. Land surface data

An evaluation of the lake and lake ice modules can be made by comparing observations of lake phenology (Walsh et al. 1998). Figure 21 shows the model lake's freeze date (Julian days after 31 August) and duration compared to the Global Lake and River Ice Phenology (GLRIP) database (Benson and Magnuson 2000). Cov-

January Zonal U-Wind (m/s)

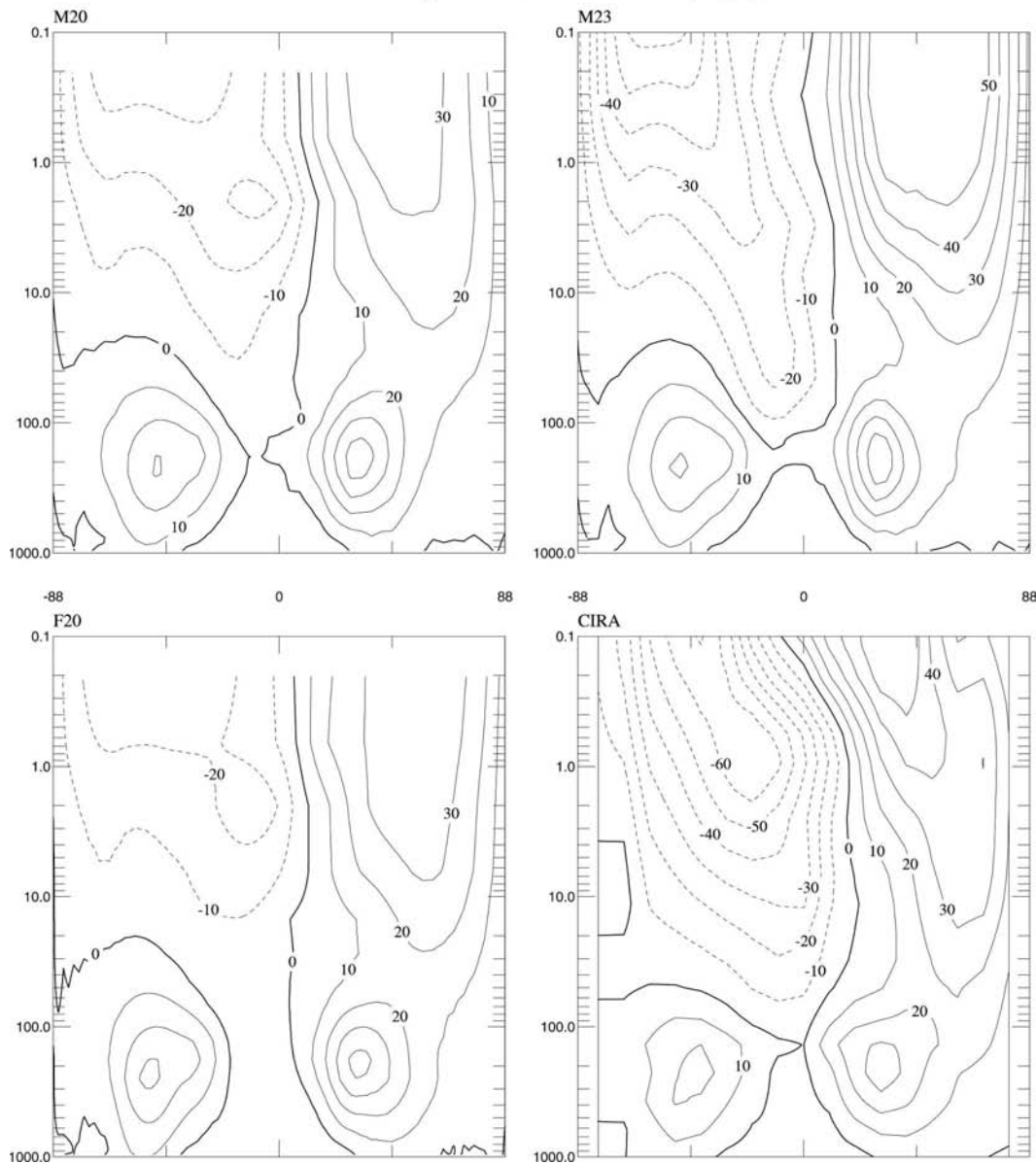


FIG. 16. Same as in Fig. 15, but for zonal mean zonal velocity.

erage of lakes is less extensive in the observations because of the small lake fraction in most areas. Only the Northern Hemisphere (NH) is shown since there is very little data for lakes in the Southern Hemisphere. In general, the pattern of lake ice freezing is consistent, but the onset of ice is generally a month earlier (and lasts a month longer) than observed. This could be due to insufficient mixing in the lakes, or possibly to the definition of when lakes freeze. In the model diagnostic, this is defined as the first time that ice appears in the season, regardless of whether it subsequently melts and refreezes.

Runoff from the major rivers can be compared to observational data (Milliman and Meade 1983; Table 4). In the Tropics, runoff is slightly deficient in the Amazon basin (due to insufficient rainfall) but overabundant in the African and Asian rain forest. High-latitude rivers are more consistently modeled.

h. Annular modes

These runs were performed with climatological SST fields (see section 3b), and so any interannual or monthly variability is purely intrinsic to the atmosphere. We highlight the model simulations of the

Surface Air Temperature (C)

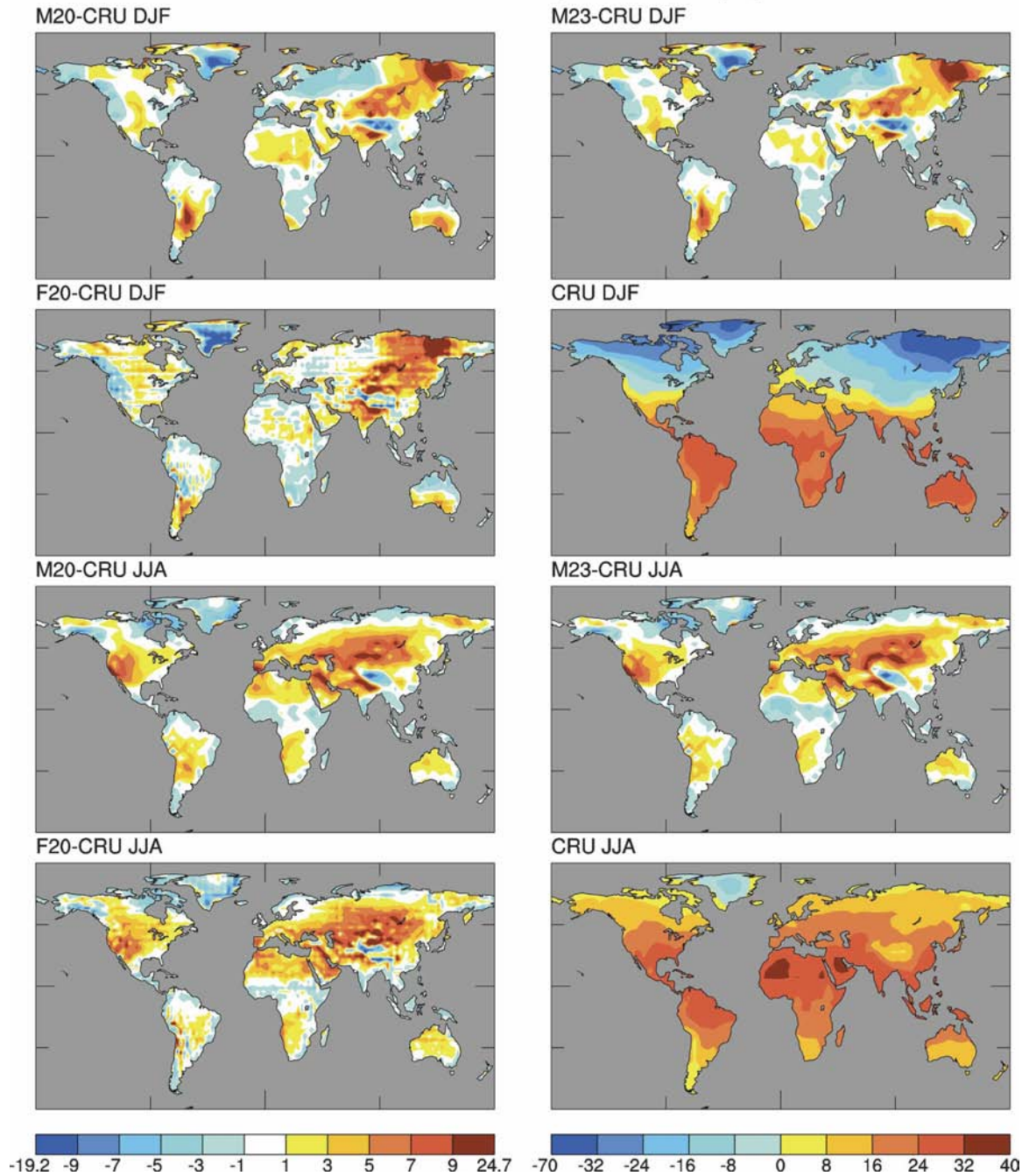


FIG. 17. SAT anomalies compared to the CRU dataset (Jones et al. 1999 and updates) for the DJF and JJA seasons.

northern annular mode (NAM) defined from the first empirical orthogonal function (EOF) of the sea level pressure field poleward of 20° (Thompson and Wallace 1998). The NAM explains 21%–23% of the wintertime (November–April) variability in all model configurations and observations (Fig. 22). The integrated value

of the EOF pattern poleward of 60° is scaled to be exactly -1 . Differences occur in the positioning of the subtropical centers of action, with the higher-resolution model comparing better to the observations. The standard deviation in the corresponding principal components (PCs; in hPa) is 3.0 hPa (in the detrended obser-

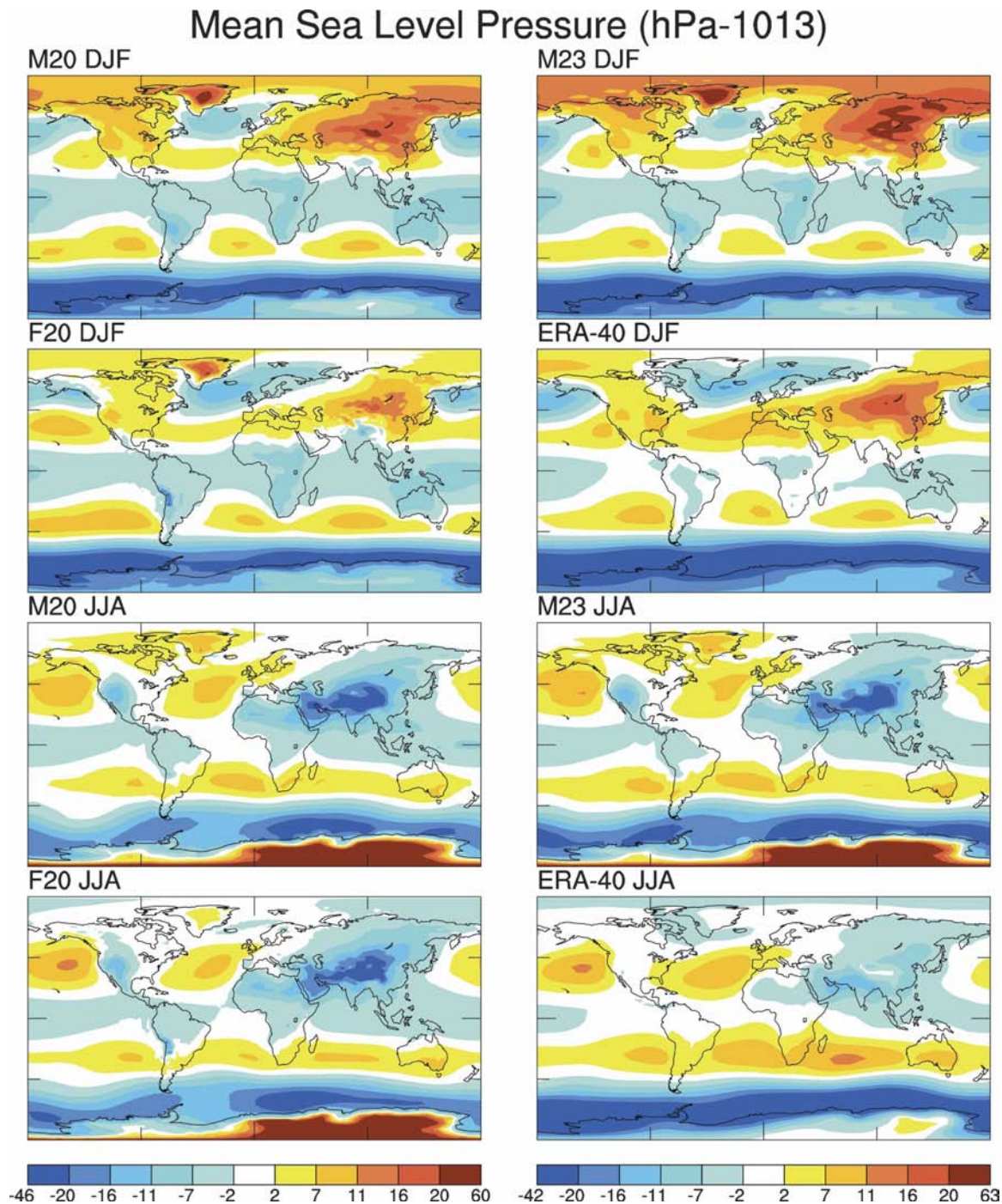


FIG. 18. SLP anomalies (from 1013 hPa) for the DJF and JJA seasons compared to ERA-40.

variations) compared to 3.7, 3.4, and 2.5 hPa in the M20, M23, and F20 runs, respectively. However, note that some variability of these patterns occurs as a function of time period and months used in the analysis. The southern annular mode, defined analogously, explains

about 29%–35% of the variance in each run and has much less variation in pattern among the models (not shown). The standard deviations in the PCs range from 3.6 to 3.9 hPa.

Other aspects of atmospheric variability (such as the

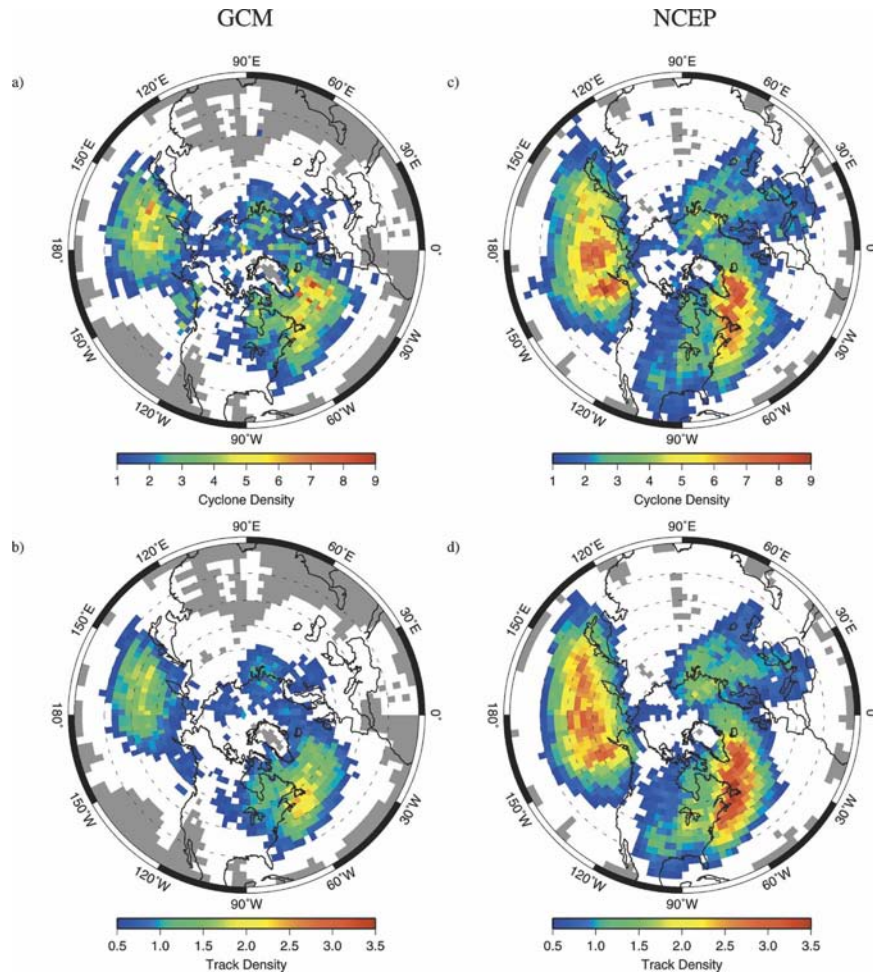


FIG. 19. (top) Storm-track frequency and (bottom) density calculated from 3-hourly data from the M23 model compared to storm tracks calculated from the NCEP reanalysis using an SLP minima tracking algorithm (Chandler and Jonas 2004).

response to tropical Pacific SST in AMIP-style simulations, or higher-frequency variability like the Madden-Julian oscillation) will be described in future papers.

6. Climate sensitivity

This paper is mainly concerned with the fidelity of the ModelE simulations of present-day climate. However, the generic climate sensitivity of the model is a function of the base state and is a useful metric to estimate the response of the model to more specific forcings. Accordingly, we use the q -flux model (with a maximum mixed layer depth of 65 m to reduce computation time) to estimate the climate response to $2\times \text{CO}_2$ and 2% reduction in the solar constant, which are roughly comparable (4.12 and -4.69 W m^{-2} adjusted forcing at the tropopause, respectively) but of opposite sign. The M20 model warms by 2.6°C for doubled CO_2

and cools by 2.8°C in the reduced solar case, giving a sensitivity of $\approx 0.6^\circ\text{C} (\text{W m}^{-2})^{-1}$. With a preindustrial base case (1880 conditions), which has slightly increased sea ice, the doubled CO_2 sensitivity is slightly larger, 2.7°C . The F20 and M23 models have sensitivities to $2\times \text{CO}_2$ of 2.8° and 2.4°C , respectively.

7. Comparison to GISS SI2000

Recent GISS publications have used SI2000 (Hansen et al. 2002) and similar configurations of Model II' (Koch et al. 1999; Menon et al. 2002; Yao and Del Genio 2002; among others). To track the improvements to the climatology, we use a selected set of well-observed data (including many of the fields discussed above) and use Taylor diagrams (Taylor 2001) to compare the model means, spatial variability, and coherence with observations (note that some fields were not

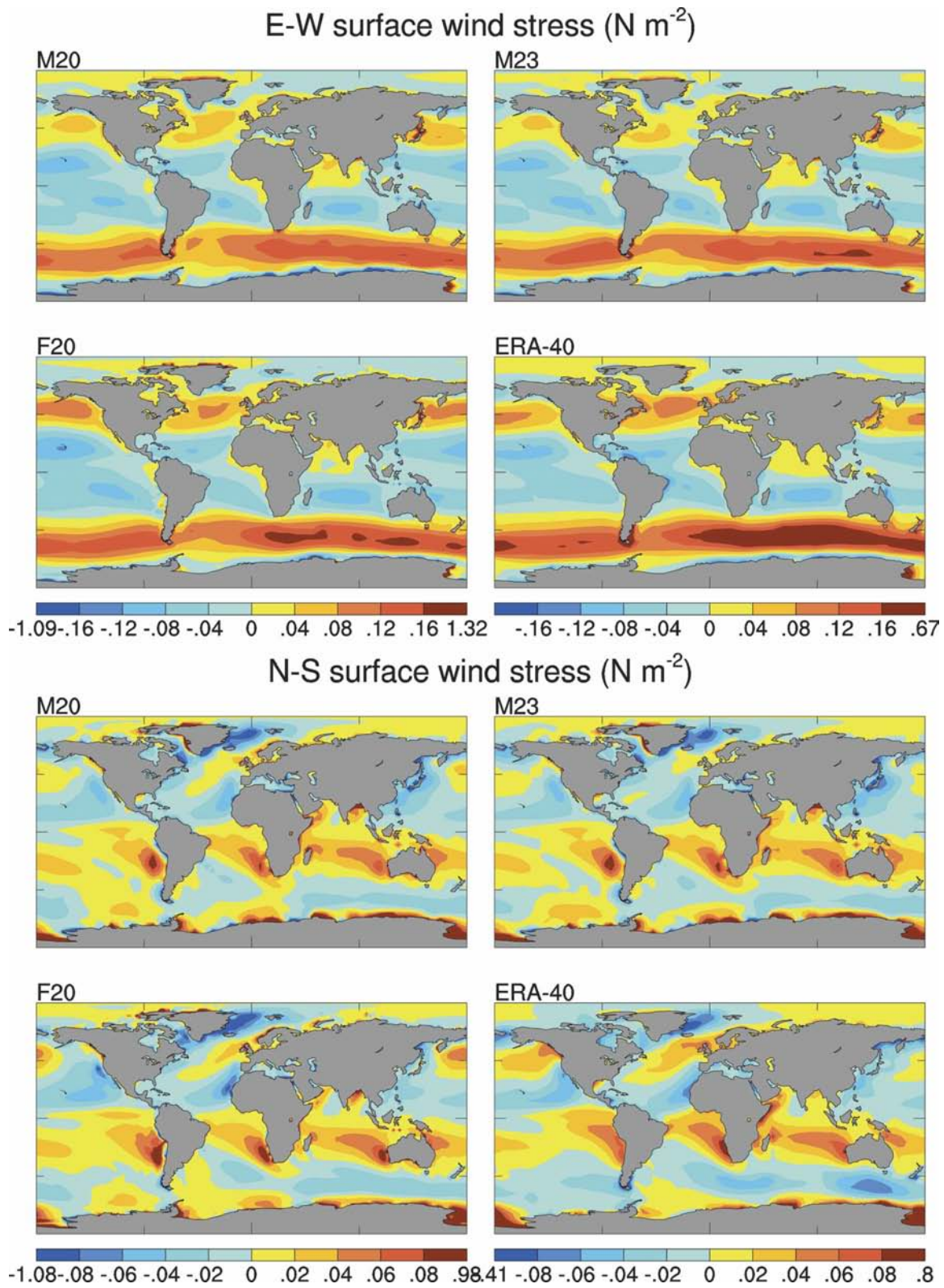


FIG. 20. Annual mean east-west and north-south ocean wind stress (N m^{-2}) compared to ERA-40.

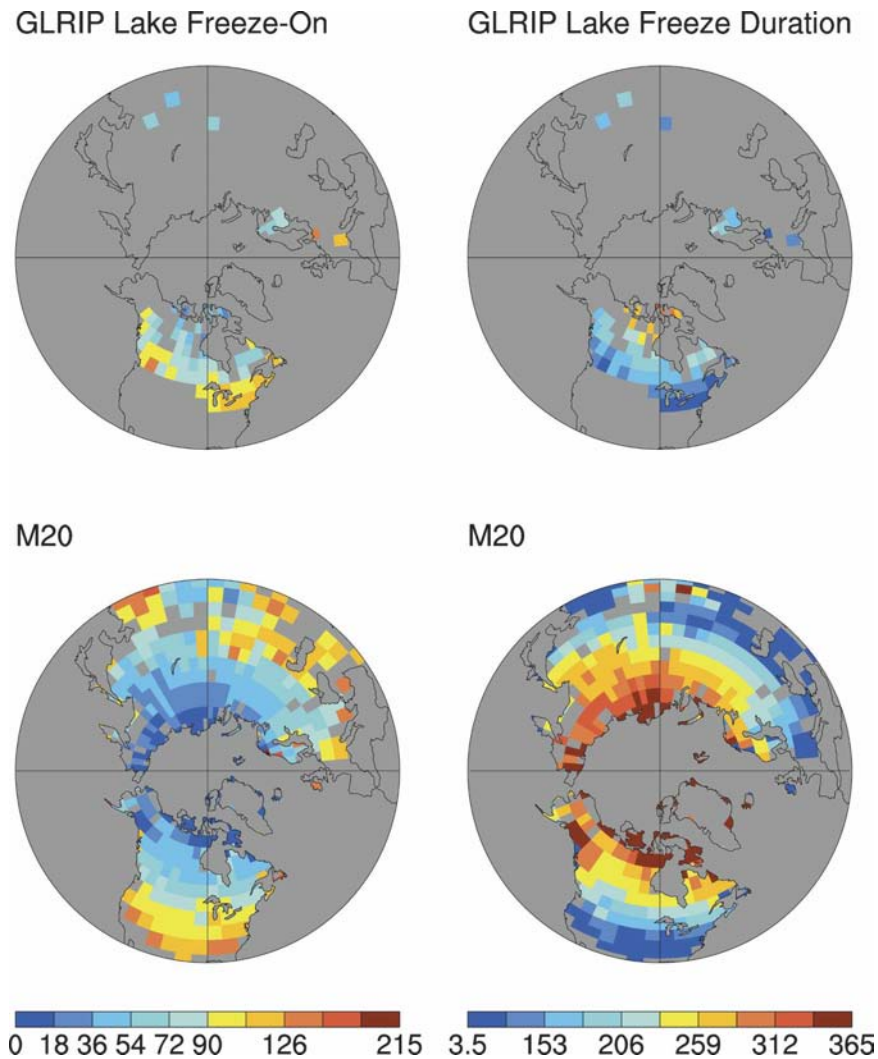


FIG. 21. Date of first lake ice and the duration of the ice in M20 and in the GLRIP database (Benson and Magnuson 2000).

available from the SI2000 simulation). An additional useful statistic is the Arcsin–Mielke (AM) score (Watterson 1996), which corresponds closely to the “best” model in these diagrams “by eye,” but addition-

ally takes into account the mean bias. Graphically, lines of constant AM score are semicircles on the Taylor diagram with centers on the x axis that move to the right as the score decreases, and with radii that decrease with the score and with increasing bias. A perfect score (unity) corresponds to the observations point, while a score of zero corresponds to the (vertical) zero correlation line.

Figure 23 shows comparisons among the selected models for the December–February (DJF) and June–July (JJA) extratropical NH CRU surface air temperature (SAT), GPCP precipitation (60°S–60°N), Remote Sensing Systems, Inc. (RSS), MSU channels 2 and 4, ISCCP total cloud and low cloud amounts (calculated using the ISCCP simulator, 60°S–60°N), the TOA LW and SW fluxes and the SW cloud radiative forcing (ERBE, 60°S–60°N), the oceanic wind stress, and the

TABLE 4. Annual mean runoff from selected rivers. All values are in $\text{km}^3 \text{ month}^{-1}$; observations are from Milliman and Meade (1983).

River	M20	F20	M23	Obs
Amazon	291	326	280	525
Congo	126	173	171	104
Brahmaputra–Ganges	145	153	158	81
Yangtze	197	107	161	74
Lena	36	36	40	42
St. Lawrence	27	30	30	37
Ob	31	30	30	32
Mackenzie	22	21	24	25

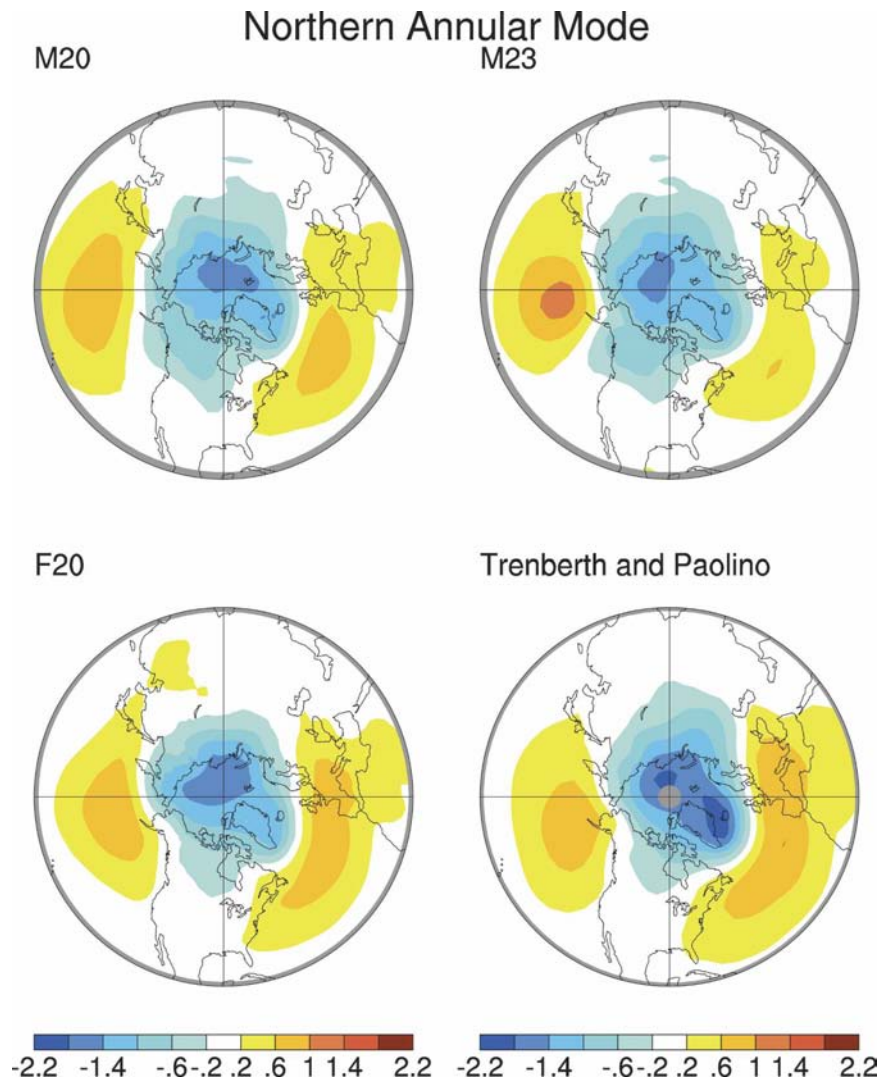


FIG. 22. The NAM derived from 10 yr+ of monthly wintertime data (November–April) compared to observations (1947–97; Trenberth and Paolino 1980 and updates). Explained variance in this first mode is 22% (M20), 21% (M23), and 23% (F20) compared to 21% (obs). Patterns are scaled so that the weighted integral from 60° to 90°N is -1 .

DJF/JJA oceanic sea level pressures (ERA-40). In each panel, different colors refer to different fields, while the symbol refers to the model simulation. In almost all cases there are improvements compared to SI2000 (the sole exception being JJA SAT), with M20 being best in most instances (here defined by a higher AM score; see Table 5). Notably, F20 is better for DJF SLP and the ocean zonal wind stress, while M23 is the best for JJA SLP. Interestingly, the results for the new models tend to cluster in comparison with SI2000, indicating that the physics they have in common is more of a determinant of their performance than the differing resolutions.

Overall, temperature-related diagnostics are better modeled than hydrological variables (precipitation and clouds). The biggest improvements have come in the dynamical fields (wind stress and SLP) where the correlations, bias, and rms error have all improved. We attribute this to improvements to the stratospheric circulations (due to a higher model top and reduced drag) and the removal of spurious angular momentum losses due to upper-atmospheric processes. Improvements in the MSU diagnostics are also a strong function of an improved middle-atmosphere simulation. Improvements in precipitation occurred as a function of the shortening of the physics time step (from 1 h to 30 min)

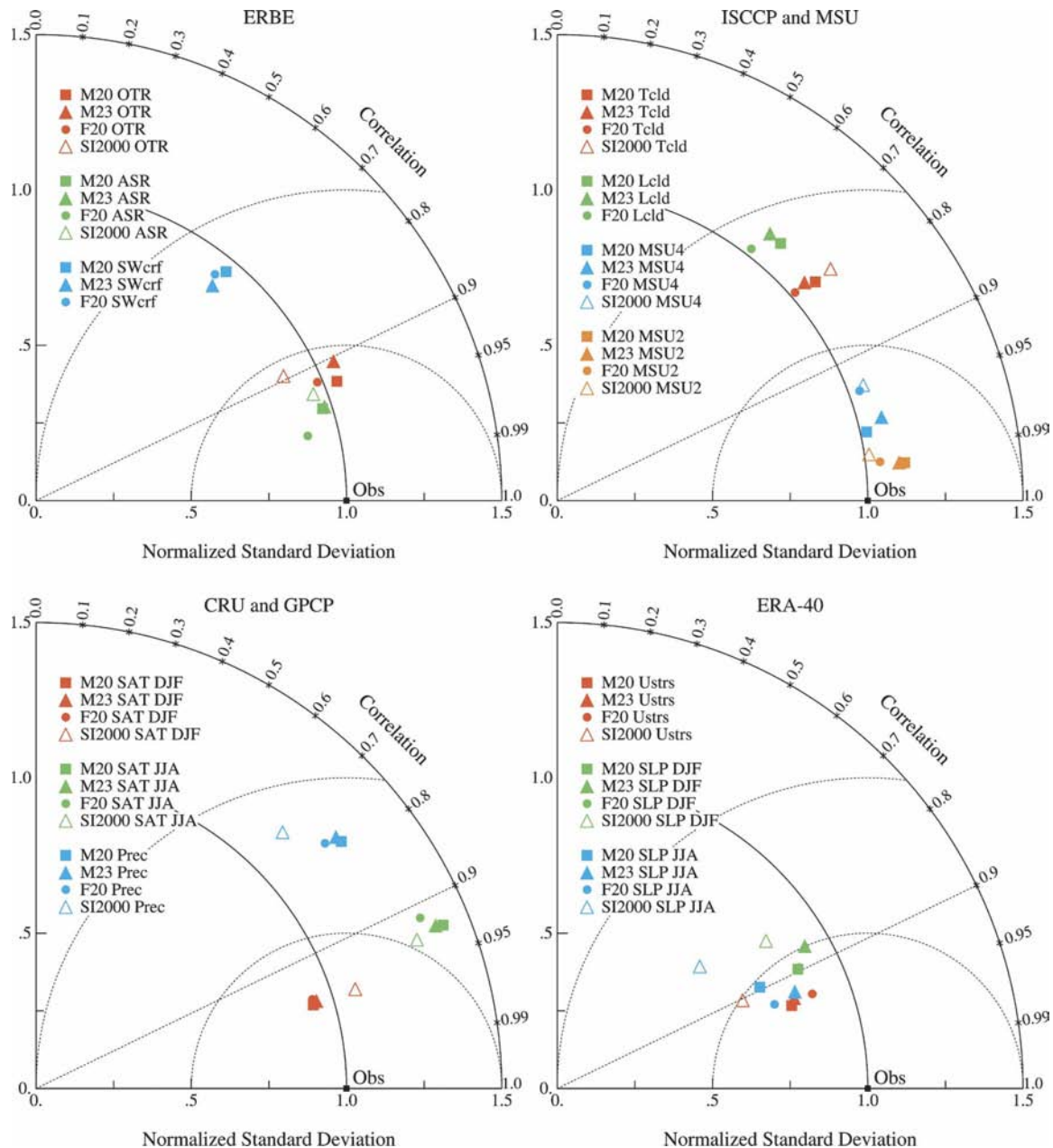


FIG. 23. Taylor diagrams for selected quantities showing the difference in performance for different model configurations. Different colors are for different fields, while different symbols are used for each model configuration: (a) ERBE: outgoing thermal radiation (OTR), absorbed solar radiation (ASR), and SW cloud radiative forcing (SWcrf); (b) ISCCP and MSU: total cloud (Tld), low cloud (Lld), and MSU-4 and MSU-2; (c) CRU and GPCP: SAT (DJF and JJA) and precipitation (Prec); (d) ERA-40: east-west ocean wind stress (Ustrs) and SLP (DJF and JJA).

and the removal of precipitation hotspots related to high topography (section 3d). Cloud improvements in the planetary boundary layer are principally due to the use of the nonlocal turbulent mixing parameterization, which lifted the humidity maximum from the lowest layer to around 900 hPa in the Tropics (section 3h). Regional improvements in SAT were also seen as a

response to the new canopy conductance model [section 3j(2)].

8. Conclusions

We have presented results from three configurations from the latest version of GISS ModelE. Despite dif-

TABLE 5. Arcsin–Mielke scores for selected fields (see Fig. 23 for field definitions). The highest score for each field is in boldface (taking account of precision not necessarily reflected in the table).

Field	M20	F20	M23	SI2000
OTR	0.72	0.71	0.67	0.69
ASR	0.80	0.84	0.80	0.76
SWcrf	0.44	0.43	0.43	—
Tcld	0.41	0.37	0.41	0.38
Lcld	0.45	0.42	0.42	—
SAT (DJF)	0.81	0.79	0.80	0.80
SAT (JJA)	0.63	0.62	0.63	0.70
Prec	0.53	0.52	0.52	0.48
Ustrs	0.72	0.74	0.72	0.61
SLP (DJF)	0.69	0.69	0.66	0.59
SLP (JJA)	0.65	0.70	0.72	0.47
MSU4	0.83	0.77	0.79	0.76
MSU2	0.90	0.90	0.90	0.83

ferences in resolution (and stratospheric physics for M23), many results are very robust. In particular, global mean quantities and the radiation budgets are extremely similar from one model to the other. Some differences are seen in the hydrological cycle, but while there are improvements in the F20 model (particularly in equatorial and storm-track regions), global-scale fields are not obviously significantly better. Overall, the M20 model has the highest skill (based on a wide selection of AM scores relative to the observations), though this may in some part be due to the greater attention that has been paid to this model version compared to the more computationally burdensome higher-resolution model; that is, the subgrid-scale parameterizations have been better optimized for this model configuration. For applications that require good stratospheric circulation with reasonable time scales and reasonable stratospheric–tropospheric exchanges, the extra resolution and physics in the M23 configuration appear warranted, but the improvement in stratospheric representation seen in M20 compared to previous model versions still leads to a significant improvement in the dynamical aspects of stratospheric influence on the troposphere over SI2000 (Shindell et al. 2004).

There are, however, some persistent problems in all configurations that merit continued attention. Cloud cover over the marine stratocumulus regions continues to be deficient (although it is slightly improved over SI2000), and is only slightly improved at higher horizontal resolution. Amazonian precipitation remains systematically low. High clouds in general are too optically thick, but cloud cover and reflected shortwave are systematically low over the southern oceans. Additional detailed assessments of these models (particularly for cloud processes and as part of a coupled

model) and their response to forcings (in atmospheric composition and to observed SST changes) are ongoing.

Further work is being done to improve the higher-resolution simulation, which includes tuning of various parameterizations as well as investigating the impact of matched increases in the vertical resolution. Work is also progressing on incorporating the Earth System Modeling Framework (ESMF) infrastructure and coupling interfaces to improve the flexibility and interoperability of the model components, and in particular to allow for more options in the dynamical core. Model output is available on the GISS Web site, and through the IPCC AR4 model intercomparison database.

Acknowledgments. Climate modeling at GISS is supported by NASA. MSU data are produced by Remote Sensing Systems, Inc., and sponsored by the NOAA Climate and Global Change Program. Data are available online at www.remss.com. ERA-40 data are available from the European Centre for Medium-Range Weather Forecasts (ECMWF; <http://www.ecmwf.int/research/era>).

REFERENCES

- Abramopoulos, F., C. Rosenzweig, and B. Choudhury, 1988: Improved ground hydrology calculations for Global Climate Models (GCMs): Soil water movement and evapotranspiration. *J. Climate*, **1**, 921–941.
- Arakawa, A., 1972: Design of the UCLA general circulation model: Numerical simulation of weather and climate. Tech. Rep. 7, Dept. of Meteorology, University of California, Los Angeles, 116 pp.
- Bauer, M., and A. D. Del Genio, 2006: Composite analysis of winter cyclones in a GCM: Influence on climatological humidity. *J. Climate*, in press.
- Benson, B., and J. Magnuson, 2000: Global lake and river ice phenology database. National Snow and Ice Data Center/World Data Center for Glaciology, Boulder, CO. [Available online at <http://nsidc.org/data/g01377.html>.]
- Betts, A. K., and A. C. M. Beljaars, 2003: ECMWF ISLSCP-II near-surface dataset from ERA-40. Tech. Rep., ERA-40 Project Report Series 8, ECMWF, 31 pp.
- Beven, K. J., and M. J. Kirkby, 1979: A physically based variable contributing area model of basin hydrology. *Hydrol. Sci. Bull.*, **24**, 43–69.
- Bitz, C. M., and W. H. Lipscomb, 1999: An energy-conserving thermodynamic model of sea ice. *J. Geophys. Res.*, **104**, 15 669–15 677.
- Boucher, O., and T. Anderson, 1995: General circulation model assessment of the sensitivity of direct climate forcing by anthropogenic sulfate aerosols to aerosol size and chemistry. *J. Geophys. Res.*, **100**, 26 117–26 134.
- Briegleb, B. P., C. M. Bitz, E. C. Hunke, W. H. Lipscomb, and J. L. Schramm, cited 2002: Description of the Community Climate System Model version 2: Sea ice model. National Center for Atmospheric Research. [Available online at <http://www.cesm.ucar.edu/models/ccsm2.0/csim/>.]

- Brutsaert, W. H., 1982: *Evaporation into the Atmosphere*. D. Reidel, 299 pp.
- Businger, J. A., J. C. Wyngaard, Y. Izumi, and E. F. Bradley, 1971: Flux–profile relationships in the atmospheric surface layer. *J. Atmos. Sci.*, **28**, 181–189.
- Cairns, B., A. A. Lacis, and B. E. Carlson, 2000: Absorption within inhomogeneous clouds and its parameterization in general circulation models. *J. Atmos. Sci.*, **57**, 700–714.
- Canuto, V. M., and M. S. Dubovikov, 1996a: A dynamical model for turbulence. I. General formalism. *Phys. Fluids*, **8**, 571–586.
- , and —, 1996b: A dynamical model for turbulence. II. Shear-driven flows. *Phys. Fluids*, **8**, 587–598.
- Chandler, M. A., and J. Jonas, cited 2004: Atlas of extratropical storm tracks 1961–1998. [Available online at <http://www.giss.nasa.gov/data/stormtracks/>.]
- Cheng, Y., V. M. Canuto, and A. M. Howard, 2002: An improved model for the turbulent PBL. *J. Atmos. Sci.*, **59**, 1550–1565.
- Chou, M.-D., K.-T. Lee, S.-C. Tsay, and Q. Fu, 1999: Parameterization for cloud longwave scattering for use in atmospheric models. *J. Climate*, **12**, 159–169.
- Cooke, W. F., C. Liou, H. Cachier, and J. Feichter, 1999: Construction of a $1^\circ \times 1^\circ$ fossil fuel emission data set for carbonaceous aerosol and implementation and radiative impact in the ECHAM4 model. *J. Geophys. Res.*, **104**, 22 137–22 162.
- Cox, C., and W. Munk, 1956: Slopes of the sea surface deduced from photographs of sun glitter. *Bull. Scripps Inst. Oceanogr.*, **6**, 401–488.
- Cramer, W., D. W. Kicklighter, A. Bondeau, B. Moore III, G. Churkina, B. Nemry, A. Ruimy, A. Schloss, and the Participants of the Potsdam NPP Model Intercomparison, 1999: Comparing global models of terrestrial net primary productivity (NPP): Overview and key results. *Global Change Biol.*, **5**, 1–15.
- Del Genio, A. D., and M.-S. Yao, 1993: Efficient cumulus parameterization for long-term climate studies: The GISS scheme. *The Representation of Cumulus Convection in Numerical Models*, Meteor. Monogr., No. 46, Amer. Meteor. Soc., 181–184.
- , M.-S. Yao, W. Kovari, and K. K. Lo, 1996: A prognostic cloud water parameterization for general circulation models. *J. Climate*, **9**, 270–304.
- , W. Kovari, M.-S. Yao, and J. Jonas, 2005a: Cumulus microphysics and climate sensitivity. *J. Climate*, **18**, 2376–2387.
- , A. B. Wolf, and M.-S. Yao, 2005b: Evaluation of regional cloud feedbacks using single column models. *J. Geophys. Res.*, **110**, D15S13, doi:10.1029/2004JD005011.
- Dessler, A. E., 1998: A reexamination of the “stratospheric fountain” hypothesis. *Geophys. Res. Lett.*, **25**, 4165–4168.
- Dufresne, J.-L., C. Gautier, P. Ricchiazzi, and Y. Fouquart, 2002: Longwave scattering effects of mineral aerosols. *J. Atmos. Sci.*, **59**, 1959–1966.
- Ebert, E. E., J. L. Schramm, and J. A. Curry, 1995: Disposition of solar radiation in sea ice and the upper ocean. *J. Geophys. Res.*, **100**, 15 965–15 975.
- Edwards, J., and A. Slingo, 1996: Studies with a flexible new radiation code. I: Choosing a configuration for a large-scale model. *Quart. J. Roy. Meteor. Soc.*, **122**, 689–719.
- Farquhar, G. D., and T. D. Sharkey, 1982: Stomatal conductance and photosynthesis. *Annu. Rev. Plant Physiol.*, **33**, 317–345.
- Fleming, E. L., S. Chandra, J. J. Barnett, and M. Corney, 1990: Zonal mean temperature, pressure, zonal wind and geopotential height as function of latitude, COSPAR International Reference Atmosphere: 1986, Part II: Middle Atmosphere Models. *Adv. Space Res.*, **12**, 11–59.
- , C. H. Jackson, R. S. Stolarski, and D. B. Considine, 1999: Simulation of stratospheric tracers using an improved empirically based two-dimensional model transport. *J. Geophys. Res.*, **104**, 23 911–23 934.
- Fofonoff, N. P., and R. C. Millard Jr., 1983: Algorithms for computation of fundamental properties of seawater. Tech. Rep. 44, UNESCO, Technical Papers in Marine Science.
- Fowler, L. D., D. A. Randall, and S. A. Rutledge, 1996: Liquid and ice cloud microphysics in the CSU general circulation model. Part I: Model description and simulated microphysical processes. *J. Climate*, **9**, 489–529.
- Friend, A. D., and N. Y. Kiang, 2005: Land surface model development for the GISS GCM: Effects of improved canopy physiology. *J. Climate*, **18**, 2883–2902.
- Fu, Q., C. M. Johanson, S. G. Warren, and D. J. Seidel, 2004: Contribution of stratospheric cooling to satellite-inferred tropospheric temperature trends. *Nature*, **429**, 55–58.
- Ganachaud, A., and C. Wunsch, 2003: Large-scale ocean heat and freshwater transports during the World Ocean Circulation Experiment. *J. Climate*, **16**, 696–705.
- Gates, W. L., and Coauthors, 1999: An overview of the results of the Atmospheric Model Intercomparison Project (AMIP I). *Bull. Amer. Meteor. Soc.*, **80**, 29–55.
- GFDL Global Atmospheric Model Development Team, 2004: The new GFDL global atmosphere and land model AM2/LM2: Evaluation with prescribed SST simulations. *J. Climate*, **17**, 4641–4673.
- Gill, A. E., 1982: *Atmosphere-Ocean Dynamics*. Academic Press, 662 pp.
- Gordon, H. R., and M. M. Jacobs, 1977: Albedo of the ocean-atmosphere system: Influence of sea foam. *Appl. Opt.*, **16**, 2257–2260.
- Gu, L. H., D. D. Baldocchi, S. C. Wofsy, J. W. Munger, J. J. Michalsky, S. P. Urbanski, and T. A. Boden, 2003: Response of a deciduous forest to the Mount Pinatubo eruption: Enhanced photosynthesis. *Science*, **299**, 2035–2038.
- Gunn, K. L. S., and G. D. Kinzer, 1949: The terminal velocity of fall for water droplets in stagnant air. *Meteorology*, **6**, 243–251.
- Hansen, J. E., and L. Nazarenko, 2004: Soot climate forcing via snow and ice albedos. *Proc. Natl. Acad. Sci. USA*, **101**, doi:10.1073/pnas.2237157100.
- , G. L. Russell, D. Rind, P. Stone, A. Lacis, R. Ruedy, and L. Travis, 1983: Efficient three-dimensional models for climatic studies. *Mon. Wea. Rev.*, **111**, 609–662.
- , A. Lacis, D. Rind, G. Russell, P. Stone, I. Fung, R. Ruedy, and J. Lerner, 1984: Climate sensitivity: Analysis of feedback mechanisms. *Climate Processes and Climate Sensitivity*, Geophys. Monogr., No. 29, Amer. Geophys. Union, 130–163.
- , and Coauthors, 1997: Forcings and chaos in interannual to decadal climate change. *J. Geophys. Res.*, **102**, 25 679–25 720.
- , and Coauthors, 2002: Climate forcings in Goddard Institute for Space Studies SI2000 simulations. *J. Geophys. Res.*, **107**, 4347, doi:10.1029/2001JD001143.
- , and Coauthors, 2005: Efficacy of climate forcings. *J. Geophys. Res.*, **110**, D18104, doi:10.1029/2005JD005776.
- Harrison, E. F., P. Minnis, B. R. Barkstrom, V. Ramanathan, R. D. Cess, and G. G. Gibson, 1990: Seasonal variation of

- cloud radiative forcing derived from the Earth Radiation Budget Experiment. *J. Geophys. Res.*, **95**, 18 687–18 703.
- Hartke, G. J., and D. Rind, 1997: Improved surface and boundary layer models for the Goddard Institute for Space Studies general circulation model. *J. Geophys. Res.*, **102**, 16 407–16 422.
- Hogstrom, U., 1988: Non-dimensional wind and temperature profiles in the atmospheric surface layer: A re-evaluation. *Bound.-Layer Meteor.*, **42**, 55–78.
- Holland, D. M., and A. Jenkins, 1999: Modeling thermodynamic ice–ocean interactions at the base of an ice shelf. *J. Phys. Oceanogr.*, **29**, 1787–1800.
- Holtstlag, A. A. M., and C.-H. Moeng, 1991: Eddy diffusivity and countergradient transport in the convective atmospheric boundary layer. *J. Atmos. Sci.*, **48**, 1690–1698.
- , and B. Boville, 1993: Local versus nonlocal boundary-layer diffusion in a global climate model. *J. Climate*, **6**, 1825–1842.
- Houghton, J. T., Y. Ding, D. J. Griggs, M. Nougier, P. J. van der Linden, X. Dai, K. Maskell, and C. A. Johnson, Eds., 2001: *Climate Change 2001: The Scientific Basis*. Cambridge University Press, 881 pp.
- Huffman, G. J., and Coauthors, 1997: The Global Precipitation Climatology Project (GPCP) combined precipitation dataset. *Bull. Amer. Meteor. Soc.*, **78**, 5–20.
- Jain, A. K., B. P. Briegleb, K. Minschwaner, and D. J. Wuebbles, 2000: Radiative forcings and global warming potentials for 39 greenhouse gases. *J. Geophys. Res.*, **105**, 20 773–20 790.
- Jones, P. D., M. New, D. E. Parker, S. Martin, and I. Rigor, 1999: Surface air temperature and its variations over the last 150 years. *Rev. Geophys.*, **37**, 173–199.
- Keating, G. M., and D. F. Young, 1985: Interim reference ozone models for the middle atmosphere. *Middle Atmosphere Program Handbook for MAP*, K. Labitzke, J. J. Barnett, and B. Edwards, Eds., Vol. 16, ICSU Scientific Committee on Solar-Terrestrial Physics (SCOSTEP), 205–229.
- Kiehl, J. T., and K. E. Trenberth, 1997: Earth's annual global mean energy budget. *Bull. Amer. Meteor. Soc.*, **78**, 197–208.
- Klein, S. A., and C. Jakob, 1999: Validation and sensitivities of frontal clouds simulated by the ECMWF model. *Mon. Wea. Rev.*, **127**, 2514–2531.
- Koch, D., 2001: Transport and direct radiative forcing of carbonaceous and sulfate aerosols in the GISS GCM. *J. Geophys. Res.*, **106**, 20 311–20 332.
- , D. J. Jacob, and W. C. Graustein, 1996: Vertical transport of aerosols in the troposphere as indicated by ^7Be and ^{210}Pb in a chemical tracer model. *J. Geophys. Res.*, **101**, 18 651–18 666.
- , —, I. Tegen, D. Rind, and M. Chin, 1999: Tropospheric sulfur simulation and sulfate direct radiative forcing in the Goddard Institute for Space Studies general circulation model. *J. Geophys. Res.*, **104**, 23 799–23 822.
- Kull, O., and B. Kruijt, 1998: Leaf photosynthetic light response: A mechanistic model for scaling photosynthesis to leaves and canopies. *Funct. Ecol.*, **12**, 767–777.
- Lacis, A. A., and V. Oinas, 1991: A description of the correlated k distribution method for modeling nongray gaseous absorption, thermal emission and multiple scattering in vertically inhomogeneous atmospheres. *J. Geophys. Res.*, **96**, 9027–9063.
- Lean, J., 2000: Evolution of the sun's spectral irradiance since the Maunder Minimum. *Geophys. Res. Lett.*, **27**, 2425–2428.
- Lefohn, A. S., J. D. Husar, and R. B. Husar, 1999: Estimating historical anthropogenic global sulfur emission patterns for the period 1850–1990. *Atmos. Environ.*, **33**, 3435–3444.
- Lioussé, C., J. E. Penner, C. Chuang, J. J. Walton, H. Eddleman, and H. Cachier, 1996: A global three-dimensional model study of carbonaceous aerosols. *J. Geophys. Res.*, **101**, 19 411–19 432.
- Liston, G. E., and D. K. Hall, 1995: An energy-balance model for lake-ice evolution. *Ann. Glaciol.*, **41**, 373–382.
- Liu, J., G. A. Schmidt, D. G. Martinson, D. Rind, G. L. Russell, and X. Yuan, 2003: Sensitivity of sea ice to physical parameterizations in the GISS global climate model. *J. Geophys. Res.*, **108**, 3053, doi:10.1029/2001JC001167.
- Locatelli, J. D., and P. V. Hobbs, 1974: Fallspeeds and masses of solid precipitation particles. *J. Geophys. Res.*, **79**, 2185–2197.
- London, J., R. D. Bojkov, S. Oltmans, and J. I. Kelly, 1976: Atlas of the global distribution of total ozone July 1957–June 1967. NCAR Tech. Rep. NCAR/TN/113+STR, 276 pp.
- Loth, B., and H.-F. Graf, 1998: Modelling the snow cover in climate studies: Part I: Long-term integrations under different climate conditions using a multi-layer snow cover model. *J. Geophys. Res.*, **103**, 11 313–11 327.
- Lucas, C., E. J. Zipser, and M. A. Lemone, 1994: Vertical velocity in oceanic convection off tropical Australia. *J. Atmos. Sci.*, **51**, 3183–3193.
- Lynch-Stieglitz, M., 1994: The development and validation of a simple snow model for the GISS GCM. *J. Climate*, **7**, 1842–1855.
- Mann, M. E., and G. A. Schmidt, 2003: Ground vs. surface air temperature trends: Implications for borehole surface temperature reconstructions. *Geophys. Res. Lett.*, **30**, 1607, doi:10.1029/2003GL017170.
- Marshall, J. S., and W. M. Palmer, 1948: The distribution of raindrops with size. *J. Meteor.*, **5**, 165–166.
- McPhee, M. G., G. A. Maykut, and J. H. Morison, 1987: Dynamics and thermodynamics of the ice/upper ocean system in the marginal ice zone of the Greenland Sea. *J. Geophys. Res.*, **92**, 7017–7031.
- Mears, C. A., M. Schabel, and F. J. Wentz, 2003: A reanalysis of the MSU channel 2 tropospheric temperature record. *J. Climate*, **16**, 3650–3664.
- Mellor, G., and T. Yamada, 1982: Development of a turbulent closure model for geophysical fluid problems. *Rev. Geophys. Space Phys.*, **20**, 851–875.
- Menon, S., A. D. Del Genio, D. Koch, and G. Tselioudis, 2002: GCM simulations of the aerosol indirect effect: Sensitivity to cloud parameterization and aerosol burden. *J. Atmos. Sci.*, **59**, 692–741.
- Miller, J. R., G. L. Russell, and G. Caliri, 1994: Continental-scale river flow in climate models. *J. Climate*, **7**, 914–928.
- Miller, R. L., I. Tegen, and J. Perlwitz, 2004: Surface radiative forcing by soil dust aerosols and the hydrologic cycle. *J. Geophys. Res.*, **109**, D04203, doi:10.1029/2003JD004085.
- Milliman, J. D., and R. H. Meade, 1983: World-wide delivery of river sediment to the oceans. *J. Geol.*, **91**, 1–21.
- Minschwaner, K., R. W. Carver, B. P. Briegleb, and A. E. Roche, 1998: Infrared radiative forcing and atmospheric lifetimes of trace species based on observations from UARS. *J. Geophys. Res.*, **103**, 23 243–23 253.
- Mishchenko, M. I., L. D. Travis, and D. W. Mackowski, 1996: T-matrix computations of light scattering by nonspherical particles: A review. *J. Quant. Spectrosc. Radiat. Transfer*, **55**, 535–575.
- Moeng, C.-H., and P. P. Sullivan, 1994: A comparison of shear- and buoyancy-driven planetary boundary layer flows. *J. Atmos. Sci.*, **51**, 999–1022.

- Naik, V., A. K. Jain, K. O. Patten, and D. J. Wuebbles, 2000: Consistent sets of atmospheric lifetimes and radiative forcings on climate for CFC replacements: HCFCs and HFCs. *J. Geophys. Res.*, **105**, 6903–6914.
- Nemesure, S., R. Wagener, and S. Schwartz, 1995: Direct short-wave forcing of climate by the anthropogenic sulfate aerosol: Sensitivity to particle size, composition, and relative humidity. *J. Geophys. Res.*, **100**, 26 105–26 116.
- Novakov, T., V. Ramanathan, J. E. Hansen, T. W. Kirchstetter, M. Sato, J. E. Sinton, and J. A. Sathaye, 2003: Large historical changes of fossil-fuel black carbon aerosols. *Geophys. Res. Lett.*, **30**, 1324, doi:10.1029/2002GL016345.
- Oinas, V., A. A. Lacis, D. Rind, D. T. Shindell, and J. E. Hansen, 2001: Radiative cooling by stratospheric water vapor: Big differences in GCM results. *Geophys. Res. Lett.*, **28**, 2791–2794.
- Palle, E., and Coauthors, 2003: Earthshine and the Earth's albedo: 2. Observations and simulations over 3 years. *J. Geophys. Res.*, **108**, 4710, doi:10.1029/2003JD003611.
- Paltridge, G. W., and C. M. R. Platt, 1976: *Radiative Processes in Meteorology and Climatology*. Elsevier, 318 pp.
- Patterson, E. M., D. A. Gillette, and B. H. Stockton, 1977: Complex index of refraction between 300 and 700nm for Saharan aerosols. *J. Geophys. Res.*, **82**, 3153–3160.
- Prather, M. J., 1986: Numerical advection by conservation of second order moments. *J. Geophys. Res.*, **91**, 6671–6680.
- Ramankutty, N., and J. A. Foley, 1999: Estimating historical changes in global land cover: Croplands from 1700 to 1992. *Global Biogeochem. Cycles*, **1**, 997–1027.
- Randel, D. L., T. H. Vonder Haar, M. A. Ringerud, G. L. Stephens, T. J. Greenwald, and C. L. Combs, 1996: A new global water vapor dataset. *Bull. Amer. Meteor. Soc.*, **77**, 1233–1246.
- Randel, W. J., and F. Wu, 1999: Cooling of the Arctic and Antarctic polar stratospheres due to ozone depletion. *J. Climate*, **12**, 1467–1479.
- Rayner, N. A., D. E. Parker, E. B. Horton, C. K. Folland, L. V. Alexander, D. P. Rowell, E. C. Kent, and A. Kaplan, 2003: Global analyses of SST, sea ice and night marine air temperature since the late nineteenth century. *J. Geophys. Res.*, **108**, 4407, doi:10.1029/2002JD002670.
- Rind, D., and J. Lerner, 1996: Use of on-line tracers as a diagnostic tool in general circulation model development. 1. Horizontal and vertical transport in the troposphere. *J. Geophys. Res.*, **101**, 12 667–12 683.
- , R. Suozzo, N. Balachandran, A. Lacis, and G. Russell, 1988: The GISS global climate–middle atmosphere model. Part I: Model structure and climatology. *J. Atmos. Sci.*, **45**, 329–370.
- , J. Lerner, K. Shah, and R. Suozzo, 1999: Use of on-line tracers as a diagnostic tool in general circulation model development. 2. Transport between the troposphere and stratosphere. *J. Geophys. Res.*, **104**, 9151–9167.
- , M. Chandler, P. Lonergan, and J. Lerner, 2001a: Climate change and the middle atmosphere. 5. Paleostratosphere in cold and warm climates. *J. Geophys. Res.*, **106**, 20 195–20 212.
- , P. Dumenocal, G. L. Russell, S. Sheth, D. Collins, G. A. Schmidt, and J. Teller, 2001b: Effects of glacial meltwater in the GISS Coupled Atmosphere–Ocean Model: Part I: North Atlantic Deep Water response. *J. Geophys. Res.*, **106**, 27 335–27 354.
- Ritter, B., and J. Geleyn, 1992: A comprehensive radiation scheme for numerical weather prediction models with potential application in climate simulations. *Mon. Wea. Rev.*, **120**, 303–325.
- Roesch, A., M. Wild, H. Gilgen, and A. Ohmura, 2001: A new snow cover fraction parametrisation for the ECHAM4 GCM. *Climate Dyn.*, **17**, 933–946.
- Rosenzweig, C., and F. Abramopoulos, 1997: Land surface model development for the GISS GCM. *J. Climate*, **10**, 2040–2054.
- Rossow, W. B., and R. A. Schiffer, 1999: Advances in understanding clouds from ISCCP. *Bull. Amer. Meteor. Soc.*, **80**, 2261–2288.
- , C. Delo, and B. Cairns, 2002: Implications of the observed mesoscale variations of clouds for the Earth's radiation budget. *J. Climate*, **15**, 557–585.
- Russell, G. L., J. R. Miller, and L.-C. Tsang, 1985: Seasonal oceanic heat transports computed from an atmospheric model. *Dyn. Atmos. Ocean*, **9**, 253–271.
- , —, and D. Rind, 1995: A coupled atmosphere–ocean model for transient climate change. *Atmos.–Ocean*, **33**, 683–730.
- , —, —, R. A. Ruedy, G. A. Schmidt, and S. Sheth, 2000: Comparison of model and observed regional temperature changes during the past 40 years. *J. Geophys. Res.*, **105**, 14 891–14 898.
- Russell, J. M., and Coauthors, 1993: The Halogen Occultation Experiment. *J. Geophys. Res.*, **98**, 10 777–10 798.
- Rutledge, S. A., and P. V. Hobbs, 1984: The mesoscale and microscale structure and organization of clouds and precipitation in midlatitude cyclones. XII: A diagnostic modeling study of precipitation development in narrow cold-frontal rainbands. *J. Atmos. Sci.*, **41**, 2949–2972.
- Sato, M., and Coauthors, 2003: Global atmospheric black carbon inferred from AERONET. *Proc. Natl. Acad. Sci. USA*, **100**, doi:10.1073/pnas.0731897100.
- Schlesinger, W., 1991: *Biogeochemistry: An Analysis of Global Change*. Academic Press, 443 pp.
- Schmidt, G. A., C. M. Bitz, U. Mikolajewicz, and L. B. Tremblay, 2004: Ice-ocean boundary conditions for coupled models. *Ocean Modell.*, **7**, 59–74.
- Schramm, J. L., J. A. Curry, M. M. Holland, and E. E. Ebert, 1997: Modeling the thermodynamics of a sea ice thickness distribution. 1. Sensitivity to ice thickness resolution. *J. Geophys. Res.*, **102**, 23 079–23 091.
- Sellers, P. J., and Coauthors, 1996: A revised land surface parameterization (SiB2) for atmospheric GCMs. Part I: Model formulation. *J. Climate*, **9**, 676–705.
- Shah, K. P., and D. Rind, 1995: Use of microwave brightness temperatures with a general circulation model. *J. Geophys. Res.*, **100**, 13 841–13 874.
- Shindell, D. T., D. H. Rind, and P. Lonergan, 1998: Increased polar stratospheric ozone losses and delayed eventual recovery due to increasing greenhouse gas concentrations. *Nature*, **392**, 589–592.
- , R. L. Miller, G. A. Schmidt, and L. Pandolfo, 1999: Simulation of recent northern winter climate trends by greenhouse-gas forcing. *Nature*, **399**, 452–455.
- , J. L. Grenfell, D. Rind, C. Price, and V. Grewe, 2001: Chemistry–climate interactions in the GISS GCM. Part 1: Tropospheric chemistry model description and evaluation. *J. Geophys. Res.*, **106**, 8047–8076.
- , G. Faluvegi, and N. Bell, 2003: Preindustrial-to-present-day radiative forcing by tropospheric ozone from improved simulations with the GISS chemistry–climate GCM. *Atmos. Chem. Phys.*, **3**, 1675–1702.
- , G. A. Schmidt, M. E. Mann, and G. Faluvegi, 2004: Dynamic winter climate response to large tropical volcanic eruptions.

- tions since 1600. *J. Geophys. Res.*, **109**, D05104, doi:10.1029/2003JD004151.
- Simmons, A. J., and J. Gibson, 2000: The ERA-40 project plan. Tech. Rep., ERA-40 Project Report Series 1, ECMWF, Reading, United Kingdom, 63 pp.
- Sinyuk, A., O. Torres, and O. Dubovik, 2003: Combined use of satellite and surface observations to infer the imaginary part of the refractive index of Saharan dust. *Geophys. Res. Lett.*, **30**, 1081, doi:10.1029/2002GL016189.
- Stephens, G. L., P. M. Gabriel, and P. T. Partain, 2001: Parameterization of atmospheric radiative transfer. Part I: Validity of simple models. *J. Atmos. Sci.*, **58**, 3391–3409.
- Sundqvist, H., 1978: A parameterization scheme for non-convective condensation including prediction of cloud water content. *Quart. J. Roy. Meteor. Soc.*, **104**, 677–690.
- , E. Berge, and J. E. Kristjansson, 1989: Condensation and cloud parameterization studies with a mesoscale numerical weather prediction model. *Mon. Wea. Rev.*, **117**, 1641–1657.
- Tang, I. N., 1996: Chemical and size effects of hygroscopic aerosols on light scattering coefficients. *J. Geophys. Res.*, **101**, 19 245–19 250.
- , and H. R. Munkelwitz, 1991: Simultaneous determination of refractive index and density of an evaporating aqueous solution droplet. *Aerosol Sci. Technol.*, **15**, 201–207.
- , and —, 1994: Water activities, densities, and refractive indices of aqueous sulfates and sodium nitrate droplets of atmospheric importance. *J. Geophys. Res.*, **99**, 18 801–18 808.
- , W. T. Wong, and H. R. Munkelwitz, 1981: The relative importance of atmospheric sulfates and nitrates invisibility reduction. *Atmos. Environ.*, **15**, 2463–2471.
- Taylor, K. E., 2001: Summarizing multiple aspects of model performance in a single diagram. *J. Geophys. Res.*, **106**, 7183–7192.
- Tegen, I., P. Hollrig, M. Chin, I. Fung, D. Jacob, and J. Penner, 1997: Contribution of different aerosol species to the global aerosol extinction optical thickness: Estimates from model results. *J. Geophys. Res.*, **102**, 23 895–23 915.
- , D. Koch, A. A. Lacis, and M. Sato, 2000: Trends in tropospheric aerosol loads and corresponding impact on direct radiative forcing between 1950 and 1990: A model study. *J. Geophys. Res.*, **105**, 26 971–26 989.
- Thompson, D. W. J., and J. M. Wallace, 1998: The Arctic Oscillation signature in the wintertime geopotential height and temperature fields. *Geophys. Res. Lett.*, **25**, 1297–1300.
- Trenberth, K. E., and D. A. Paolino, 1980: The Northern Hemisphere sea level pressure data set: Trends, errors and discontinuities. *Mon. Wea. Rev.*, **108**, 855–872.
- , and J. M. Caron, 2001: Estimates of meridional atmosphere and ocean heat transports. *J. Climate*, **14**, 3433–3443.
- Volz, F. E., 1973: Infrared optical constants of ammonium sulfate, Sahara dust, volcanic pumice and flyash. *Appl. Opt.*, **12**, 564–568.
- Waliser, D. E., Z. Shi, and J. R. Lanzante, 1999: The Hadley circulation: Assessing NCEP/NCAR reanalysis and sparse in-situ estimates. *Climate Dyn.*, **15**, 719–735.
- Walsh, S. E., S. J. Vavrus, V. A. Fisher, R. H. Wynne, and J. D. Lenters, 1998: Global patterns of lake ice phenology and climate: Model simulations and observations. *J. Geophys. Res.*, **103**, 28 825–28 837.
- Warren, S. G., and W. J. Wiscombe, 1980: A model for the spectral albedo of snow. II: Snow containing atmospheric aerosols. *J. Atmos. Sci.*, **37**, 2734–2745.
- Watterson, I. G., 1996: Non-dimensional measures of climate model performance. *Int. J. Climatol.*, **16**, 379–391.
- Webb, M., C. Senior, S. Bony, and J. Morcrette, 2001: Combining ERBE and ISCCP data to assess clouds in the Hadley Centre, ECMWF and LMD atmospheric climate models. *Climate Dyn.*, **17**, 905–922.
- Weng, F., N. C. Grody, R. R. Ferraro, A. Basist, and D. Forsyth, 1997: Cloud liquid water climatology from the Special Sensor Microwave Imager. *J. Climate*, **10**, 1086–1096.
- Xie, P., and A. Arkin, 1997: Global precipitation: A 17-year monthly analysis based on gauge observations, satellite estimates, and numerical model outputs. *Bull. Amer. Meteor. Soc.*, **78**, 2539–2558.
- Yao, M.-S., and A. D. Del Genio, 1989: Effects of cumulus entrainment and multiple cloud types on a January global climate model simulation. *J. Climate*, **2**, 850–863.
- , and A. D. Del Genio, 2002: Effects of cloud parameterization on the simulation of climate changes in the GISS GCM. Part II: Sea surface temperature and cloud feedbacks. *J. Climate*, **15**, 2491–2504.
- Zhang, J., and D. Rothrock, 2000: Modeling Arctic sea ice with an efficient plastic solution. *J. Geophys. Res.*, **105**, 3325–3338.
- Zhang, Y.-C., and W. Rossow, 1997: Estimating meridional energy transports by the atmospheric and oceanic general circulations using boundary flux data. *J. Climate*, **10**, 2358–2373.
- , W. B. Rossow, A. A. Lacis, V. Oinas, and M. I. Mishchenko, 2004: Calculation of radiative fluxes from the surface to top of atmosphere based on ISCCP and other global data sets: Refinements of the radiative transfer model and the input data. *J. Geophys. Res.*, **109**, D19105, doi:10.1029/2003JD004457.